Physics of Fluids

Secondary lock-in of vortex-induced vibration and energy transfer characteristics of a vibrating cylinder subject to cross buoyancy

Cite as: Phys. Fluids **33**, 073607 (2021); https://doi.org/10.1063/5.0056162
Submitted: 07 May 2021 • Accepted: 21 June 2021 • Published Online: 13 July 2021

Bin Liu (刘斌) and Hongjun Zhu (朱红钧)

View Online Export Citation CrossMark

ARTICLES YOU MAY BE INTERESTED IN

Wake structure and evolution of flow over a finned circular cylinder
Physics of Fluids **33**, 073613 (2021); https://doi.org/10.1063/5.0060329

Numerical investigations of three-dimensional flows around a cylinder attaching with symmetric strips
Physics of Fluids **33**, 075101 (2021); https://doi.org/10.1063/5.0055280

Effect of free-stream inclination and buoyancy on flow past a square cylinder in large-scale heating regime
Physics of Fluids **33**, 073601 (2021); https://doi.org/10.1063/5.0054766

Physics of Fluids
Special Topic: Food Physics
Submit Today!

AIP Publishing

© 2021 Author(s).

Physics of Fluids ARTICLE scitation.org/journal/phf

Secondary lock-in of vortex-induced vibration and energy transfer characteristics of a vibrating cylinder subject to cross buoyancy

Cite as: Phys. Fluids **33**, 073607 (2021); doi: 10.1063/5.0056162
Submitted: 7 May 2021 · Accepted: 21 June 2021 ·
Published Online: 13 July 2021

View Online Export Citation CrossMark

Bin Liu (刘斌),[1,a)] and Hongjun Zhu (朱红钧)[2]

AFFILIATIONS

[1]Department of Mechanical Engineering, National University of Singapore, Singapore 119077
[2]State Key Laboratory of Oil and Gas Reservoir Geology and Exploration, Southwest Petroleum University, Chengdu 610500, People's Republic of China

[a)]Author to whom correspondence should be addressed: a0098961@u.nus.edu

ABSTRACT

The hydrodynamic and thermal characteristics of a freely vibrating circular cylinder subject to cross buoyancy are numerically investigated at low Reynolds numbers. The structural responses and onset of vortex-induced vibration (VIV) are documented over a range of parameter space, $2.0 \leq$ reduced velocity $(Ur) \leq 10.0$, $0.7 \leq$ Prandtl number $(Pr) \leq 10.0$ and $0.5 \leq$ Richardson number $(Ri) \leq 2.0$. The fluid and structural coefficients are chosen as Reynolds number $(Re) = 100$, mass ratio $(m^*) = 10.0$, and damping ratio $(\zeta) = 0.01$. A phenomenon of secondary VIV lock-in is found in the cases of $Ri = 2.0$ (the cross buoyancy effect becomes influential), $Pr \lesssim 2.0$ and $Ur \gtrsim 7.0$. An extended VIV lock-in region is formed over a wide range of reduced velocity values together with a tremendous kinetic energy transfer between fluid and structure. This finding is significant for the research of hydropower harvesting. On the other hand, the influence of structural dynamics on heat convection over the surface of a heated circular cylinder is recorded and discussed as well. The significance and mutual influence between Prandtl and Richardson numbers on hydrodynamics, structural dynamics, and heat convection are discussed in detail. The temperature contours are found concentrating around the cylinder's surface in the cases of high Prandtl numbers, which are also associated with higher mean Nusselt number $(\overline{Nu})$ values. The influence on heat convection over a cylinder's surface is quantified via the computation of $\overline{Nu}$ and its fluctuation for different circumstances. The energy transfer coefficient is employed to quantify the kinetic energy transfer between the fluid and a heated structure in mixed convective flow. The phase angle difference between the transverse displacement and lift force is used to support the discussions of energy transfer in fluid.

Published under an exclusive license by AIP Publishing. https://doi.org/10.1063/5.0056162

NOMENCLATURE

A_x	Dimensionless streamwise vibration amplitude
A_y	Dimensionless transverse vibration amplitude
C_d	Drag coefficient
C_e	Energy transfer coefficient
C_l	Lift coefficient
c_p	Constant pressure specific heat
D	Characteristic length (cylinder's diameter)
f_{vs}	Vortex shedding frequency
$\boldsymbol{f}_n$	Structural frequency vector
Gr	Grashof number $(= \frac{g\beta(T_H - T_C)D^3}{\nu^2})$
g	Gravitational acceleration vector
H	Dimensionless height of computational domain
h	Surface traction vector
L_d	Dimensionless downstream distance
L_u	Dimensionless upstream distance
m^*	Mass ratio
Nu	Nusselt number
Pr	Prandtl number $(= \frac{\nu}{\alpha})$
p	Pressure
p^*	Dimensionless pressure
q	Surface heat flux
Ra	Rayleigh number $(\frac{g\beta(T_H - T_C)D^3}{\alpha\nu} = GrPr)$
Re	Reynolds number $(= \frac{U_\infty D}{\nu})$
Ri	Richardson number $(= \frac{Gr}{Re^2})$
St	Strouhal number
T	Temperature
Ur	Reduced velocity
U_∞	Freestream velocity
u	Fluid velocity vector

Published under an exclusive license by AIP Publishing

$\boldsymbol{u}^*$ Dimensionless fluid velocity vector
$\boldsymbol{u}_m^*$ Dimensionless mesh velocity vector
$\boldsymbol{x}^*$ Dimensionless coordinates
α Thermal diffusivity
β Volumetric thermal expansion coefficient
$\boldsymbol{\eta}^*$ Dimensionless displacement of structure
θ Dimensionless temperature
ν Kinematic viscosity
$\rho 0$ Reference fluid density
ζ Damping ratio
τ Dimensionless time
$\boldsymbol{\Phi}^*$ Dimensionless location of structure
ω Spanwise vorticity

I. INTRODUCTION

Thermo-physical property in fluid convection arises in many fields of science and engineering, e.g., nuclear reactors, turbine engines, fuel cells, solar energy collectors, thermal power plants, and life science research. The conservation equations describing energy transport in fluid were well developed[1–3] *a priori*. The strong temperature gradient induces heat convection in fluid convection and perturbs the surrounding hydrodynamic stability. Although a number of analytical solutions to heat transfer are available,[4,5] the geometry and boundary conditions in many practical problems are so complicated that an analytical solution is hardly possible. Hence, the numerical solutions were sought-after by the research scientists in order to explore the subtle physics in thermo-fluids.[6–10]

In many engineering applications, the flow over a circular cylinder is a canonical form used to acquire the fundamental understanding of fluid dynamics and heat transfer. In contrast to the isothermal fluid flow, the non-trivial buoyancy action in mixed convective flow can perturb local hydrodynamic stability and result in complicated flow regimes in wake. In 1990, Biswas *et al.*[11] documented unsteady mixed convection over a square obstacle in a horizontal channel. Their results show that the mixed convective flow can initiate periodicity and asymmetry in wake at low Reynolds numbers in contrast to the forced convection flow. Sanitjai and Goldstein[12] investigated the thermal characteristics over a rigid cylinder in forced convection for $2 \times 10^3 < Re < 9 \times 10^4$ and $7 < Pr < 176$, where the fluid inertia is dominant over the buoyancy action in flow. More recently, Juncu[13] numerically investigated the heat transfer characteristics in the forced convection flow over two tandem cylinder for $1 < Re < 30$ and $0.1 < Pr < 100$. It was reported that the heat convection in the evolution of flow system for $RePr > 1$ is completely different than that for $RePr < 1$. Biswas and Sarkar[14] found that hydrodynamic instabilities in the wake behind a heated cylinder grow, and flow becomes unsteady periodic if the fluid is severely influenced by buoyancy action.

In the previous studies, the primary focus is the characteristics of heat convection in flow over a stationary cylinder. However, the intensive structural motions in flow have a tremendous influence on hydrodynamics in fluid-structure interaction (FSI) problem. The subtle interaction between structural dynamics, hydrodynamics, and heat convection subject to buoyancy action is still a subject undergoing intense study. In isothermal incompressible flow, many well-documented numerical investigations[15–23] had been published to assess the complicated coupling of fluid and structural dynamics. Furthermore, in multibody systems, e.g., side-by-side,[24–28] tandem,[29–31] near-wall,[32–34] or array[35,36,62] configurations, the interference could be extremely complex and subtly associated with hydrodynamic instabilities. In this study, the primary focus is to study the effect of cross thermal buoyancy and heat convection on the hydrodynamic and structural stability, which are the key aspects in many engineering applications. It is well documented by scientists that the heat energy transfer in convection flow has an enormous impact on hydrodynamic stabilities[37–40] and the associated structural dynamics for submerged bodies. Recently, Izadpanah *et al.*[41] conducted study on heat convection around a circular cylinder vibrating in transverse direction. They noticed a beating phenomenon for $Ur = 4.0$, $\zeta = 0.05$, which leads to variations of vibration magnitude and Nusselt number in time domain. Garg *et al.*[42] numerically investigated the effect of thermal buoyancy on structural and wake stability. They observed elongated and widened vortices and isotherms in the presence of the thermal buoyancy. They also found multiple strong even and odd harmonic modes of the fundamental frequency of lift force. In 2019, Garg *et al.*[43] again studied the influence of cross-buoyancy in near-wake stability and the cylinder's transverse vibration. They concluded that a strong galloping phenomenon (the structure's vibration grows proportionally with reduced velocity) occurred for the parameter range $Ri \in [3.0, 4.0]$ and $Re = [50, 150]$. In 2020, Kan *et al.*[44] conducted a numerical investigation for a freely vibrating square cylinder in forced convection. Yang *et al.*[45] also documented a study of freely vibrating circular cylinder in the forced convection flow. To complement the aforementioned studies, a detailed investigation of the cylinder's streamwise vibration and energy transfer characteristics is emphasized in this article. Furthermore, for the first time, a secondary vortex-induced vibration (VIV) lock-in of a freely vibrating cylinder is documented in this study based on the analyses of streamwise and transverse vibrations and frequency domain. We are very interested in the effect of cross buoyancy (buoyancy action normal to fluid flow) on fluid wake and structural stability in mixed convective flow where the conservation equations of momentum and energy are strongly coupled via Boussinesq approximation (BA). In particular, the hydrodynamics of a square cylinder are significantly different from a circular cylinder because of the fixed separation points of boundary layers and the occurrence of galloping in post-VIV lock-in-state. In particular, we would like to know more about the relationships between cross buoyancy effect, fluid, and structure stabilities. To the knowledge of the authors, this research has not been documented in literature previously. Hence, the primary focuses in this article are to address the following questions:

- How does the structural dynamics accommodate itself subject to cross buoyancy in mixed convective flow, e.g., the response of VIV lock-in?
- What is the influence of structural dynamics on heat convection over a vibrating cylinder subject to cross buoyancy?
- How does cross buoyancy interfere with the kinetic energy transfer between fluid and structure?

Furthermore, the kinetic energy transfer between fluid and structure is a primary concern in hydropower harvesting. Liu and Jaiman[46] recorded that the maximum energy transfer occurs at about 90° phase angle difference between the lift force and transverse vibration during VIV lock-in. For 90° phase angle difference, the transverse motion acquires the maximum acceleration from the lift force. In contrast, the energy transfer is almost suppressed during pre- and post-lock-in regions for a vibrating cylinder in isothermal flow.[46] In this article, we further noticed a secondary VIV lock-in-state and an enhanced kinetic energy transfer between fluid and structure subject to cross buoyancy in mixed convective. It is again confirmed in this study that the maximum kinetic

Published under an exclusive license by AIP Publishing

energy transfer occurs for the phase angle difference of 90° between lift force and transverse vibration.

It is known that the buoyancy effect originates from strong temperature gradients in flow, which occurs in common flow situations. However, its significance can be very dependent on flow regimes. In forced convection, the natural convection is negligible at $Ri \lesssim 0.1$. In contrast, the natural convection becomes dominant at $Ri \gtrsim 10$ instead. On the other hand, both forced and natural convection are significant in mixed convection ($0.1 \lesssim Ri \lesssim 10$). For Richardson numbers less than 0.15, the flow was characterized by broadening of the wake; whereas Richardson numbers greater than 0.15 revealed separation delay and attached twin vortices behind the cylinder.[14] The variation of Richardson number signifies the influence of buoyancy action on fluid inertia during the transport of fluid momentum. In this investigation, we are more interested in the onset of perturbation of cross buoyancy imposed on vortex dynamics in wake. Hence, the range of Richardson number is chosen relatively close to the forced convection flow regime, $Ri = [0.5, 2.0]$. On the other hand, as Prandtl number quantifies the diffusivity of fluid momentum over heat energy, it plays a significant role in determining the heat convection and hydrodynamic characteristics in the near wake for mixed convective flow. To investigate these influences of Prandtl number (Pr) and Richardson number (Ri), the values of Pr and Ri are chosen as $0.7 \leq Pr \leq 10.0$ and $0.5 \leq Ri \leq 2.0$, respectively, considering their practical significance.

The structure of this article is organized as follow. At first, the governing equations and the derived numerical formulations are introduced in Sec. II. Following that, the setup of computational domain and the validation of derived numerical formulations are presented in Sec. III. Subsequently, the obtained numerical results of structural dynamics, hydrodynamics, and kinetic energy transfer in mixed convective flow are discussed in Sec. IV. Finally, the conclusion is drawn in Sec. V.

II. GOVERNING EQUATION AND NUMERICAL FORMULATION

In the current problem, the fluid density is assumed to be uniform, except for regions with a significant influence of buoyancy. This assumption leads to Boussinesq Approximation (BA), where the deviation of local fluid density is taken as a function of temperature difference. In mixed convection, the influence of buoyancy action on fluid inertia is non-negligible. To this end, the unsteady Navier–Stokes equation (conservation of fluid momentum) is strongly coupled with the conservation of energy to simulate heat convection and buoyancy action in flow. The unsteady Navier–Stokes equation is spatially discretized with 4-nodes quadrilateral elements in a stabilized finite element formulation. The fluid-structure interaction is precisely tracked with the body-conformal boundary layer meshes in arbitrary Lagrangian-Eulerian (ALE) description. The fluid solver is coupled with the structural solver using a second-order staggered-partitioned weakly coupling fluid-structure interaction scheme.[47] The unconditionally stable second-order accurate generalized-α time integration schemes are employed for both fluid and structure solvers to march the solutions in time. In this section, the relevant variables are explained at appropriate locations in the paragraphs. For the detailed description of the other variables, please refer to the nomenclature in this article.

A. Governing equations and non-dimensionalization

The unsteady incompressible Navier–Stokes equation in its conservative form is strongly coupled with the conservation of energy via Boussinesq approximation in Eq. (1) to simulate the mixed convective flow over an elastically mounted cylinder, where $\boldsymbol{g} = [0, -g]' = [0, -9.81]'$ is the gravitational acceleration vector. Reciprocally, the conservation of energy is strongly coupled with Navier–Stokes equation via the nonlinear advection term $[(\boldsymbol{u} \cdot \nabla)T]$. The superscript $(')$ is a transpose operator. The $\boldsymbol{u}$, p, and T are the fluid velocity vector, pressure, and temperature, respectively. α represents the thermal diffusivity. Equations (1d) and (1e) are the boundary conditions prescribed by the Dirichlet (Γ_D) and Neumann (Γ_N) domain boundaries, respectively, where $\tilde{\boldsymbol{h}}$ and $\tilde{q}$ refer to the prescribed surface traction vector and heat flux. Equation (1f) is the initial states of the flow field,

$$\nabla \cdot \boldsymbol{u} = 0, \qquad \forall \boldsymbol{x} \in \Omega^f(t), \tag{1a}$$

$$\rho_0(\partial_t \boldsymbol{u} + (\boldsymbol{u} \cdot \nabla)\boldsymbol{u}) = \nabla \cdot \boldsymbol{\sigma}\{\boldsymbol{u}, p\} + \rho \boldsymbol{g}, \qquad \forall \boldsymbol{x} \in \Omega^f(t), \tag{1b}$$

$$\partial_t T + (\boldsymbol{u} \cdot \nabla)T = \alpha \nabla^2 T, \qquad \forall \boldsymbol{x} \in \Omega^f(t), \tag{1c}$$

$$\boldsymbol{u} = \tilde{\boldsymbol{u}};\ T = \tilde{T}, \qquad \forall \boldsymbol{x} \in \Gamma_D^f(t), \tag{1d}$$

$$\boldsymbol{\sigma}\{\boldsymbol{u}, p\} \cdot \boldsymbol{n} = \tilde{\boldsymbol{h}};\ \alpha(\nabla T) \cdot \boldsymbol{n} = \tilde{q}, \qquad \forall \boldsymbol{x} \in \Gamma_N^f(t), \tag{1e}$$

$$\boldsymbol{u} = \tilde{\boldsymbol{u}}_0;\ T = \tilde{T}_0, \qquad \forall \boldsymbol{x} \in \Omega^f(0). \tag{1f}$$

The term $\partial_t(\cdot)$ refers to the time derivative of a variable with respect to the spatial coordinates ($\boldsymbol{x}$). The Cauchy stress tensor ($\boldsymbol{\sigma}$) is defined as

$$\boldsymbol{\sigma}\{\boldsymbol{u}, p\} = -p\boldsymbol{I} + 2\mu\epsilon(\boldsymbol{u}), \tag{2a}$$

$$\varepsilon(\boldsymbol{u}) = \frac{1}{2}\left[\nabla \boldsymbol{u} + (\nabla \boldsymbol{u})'\right], \tag{2b}$$

where p, $\boldsymbol{I}$, μ, and $\epsilon(\boldsymbol{u})$, respectively, are the fluid pressure, the identity matrix, the dynamic viscosity, and the strain rate tensor. Natural convection is generated by the density difference induced by the temperature differences within a fluid system. Because of the small density variations present in these types of flows, a general incompressible flow approximation is normally adopted. Assuming the density is a function of temperature, $\rho = \rho(T)$, elementary thermodynamics states that $\beta = -\frac{1}{\rho}(\partial\rho/\partial T)_p$. Hence, the density of fluid at constant pressure depends on temperature, which can be written as

$$\rho = \rho_0[1.0 - \beta(T - T_C)], \tag{3}$$

where ρ_0 is the reference fluid density. These considerations lead to the Boussinesq approximation in the y-component of conservation of momentum (along gravitational direction).

Mixed convection is a state that both buoyancy action and fluid inertia are significant. Since the flow is partially dominated by fluid inertia, a reference velocity (U_∞) value is usually known. Introducing the following dimensionless groups in Eq. (4), where U_∞ is available, the governing equations in Eq. (1) can be recast into the following dimensionless form in Eq. (5), where $\boldsymbol{n}_g = [0, -1]'$ is the unit vector of gravitational force:

$$\boldsymbol{x}^* = \frac{\boldsymbol{x}}{D}; \quad \boldsymbol{u}^* = \frac{\boldsymbol{u}}{U_\infty}; \quad \tau = \frac{tU_\infty}{D}; \tag{4a}$$

$$p^* = \frac{p + \rho_0 g z}{\rho_0 U_\infty^2}; \quad \theta = \frac{T - T_C}{T_H - T_C}. \tag{4b}$$

In Eqs. (4a) and (4b), the superscript $(*)$ indicates the proposed dimensionless groups. τ and θ, respectively, are the dimensionless time and temperature. T_H and T_C represent the highest and coolest temperature in the computational domain. The value of z is the elevation height in the direction of gravitational acceleration.

Published under an exclusive license by AIP Publishing

B. Numerical formulations of fluid-structure interaction simulation

The numerical formulation is derived by spatially discretizing the governing equations of their primitive variables in Eq. (5) using a stabilized finite element formulation at first. The spatial discretization results in a semi-discrete ordinary differential equation (ODE) in time. Similar to the conservation of momentum, the conservation of energy in Eq. (5c) involves a nonlinear advection term $(\boldsymbol{u}^* \cdot \nabla)\theta$ too, causing spurious oscillations in fluid velocity. Hence, residual-based stabilized finite element formulations, Galerkin Least Squares (GLS)[48] and Pressure Stabilizing Petrov Galerkin (PSPG),[49] are employed to stabilize the spurious oscillation in fluid velocity by introducing numerical diffusion and circumventing the Ladyzhenskaya–Babuska–Brezzi (LBB) condition of coupled velocity-pressure field. In finite element formulations, we define the appropriate sets of finite trial solution spaces (S_u^h, S_θ^h, and S_p^h) for fluid velocity, temperature, and pressure, and the corresponding finite test function spaces (V_u^h, V_θ^h, and V_p^h), respectively, where the superscript (h) indicates a finite function space, e.g., $S_u^h \subset S_u$. Hence, the stabilized finite element formulation of Eq. (5) can be written as follows: for all $\boldsymbol{\psi}_u^h \in V_u^h, \psi_p^h \in V_p^h, \psi_\theta^h \in V_\theta^h$, find $\boldsymbol{u}^{*h} \in S_u^h, p^{*h} \in S_p^h, \theta^h \in S_\theta^h$ such that Eq. (6) is satisfied.

$\mathscr{B}_G([\boldsymbol{\psi}_u^h, \psi_p^h], [\boldsymbol{u}^{*h}, p^{*h}, \theta^h])$, $\mathscr{B}_G(\psi_\theta^h, [\boldsymbol{u}^{*h}, \theta^h])$, and $\mathscr{B}_G(\psi_\theta^h, \theta^h)$ are derived from the unsteady and incompressible Navier–Stokes equation and the conservation of energy based on the standard Galerkin method in the finite element framework. The boundary integral $\mathscr{B}_{corr}(\boldsymbol{\psi}_u^h, \boldsymbol{u}^{*h})$ is a correction term[50] for the "do-nothing" outflow boundary condition to avoid the reverse numerical flux. $\mathscr{B}_S([\boldsymbol{\psi}_u^h, \psi_p^h], [\boldsymbol{u}^{*h}, p^{*h}, \theta^h])$ and $\mathscr{B}_S(\psi_\theta^h, [\boldsymbol{u}^{*h}, \theta^h])$ are the stabilization terms based on the GLS and PSPG formulations. The term $\partial_\tau(\cdot)|_{\mathscr{X}}$ refers to the spatial time derivative with respect to the fixed referential coordinates $(\mathscr{X})$ and the dimensionless time (τ) in ALE description. In Eq. (6), the nonlinear incompressible Navier–Stokes equation and conservation of energy are linearized by Newton linearization to achieve quadratic convergence, and the solution at each time step is updated in iterations until convergence. The variable $\boldsymbol{u}_n^{*h}$ and θ_n^h, respectively, refer to the velocity and temperature solutions in the last iteration. Upon convergence, the terms $((\boldsymbol{u}_n^{*h} - \boldsymbol{u}_m^{*h}) \cdot \nabla)\boldsymbol{u}^{*h} + ((\boldsymbol{u}^{*h} - \boldsymbol{u}_m^{*h}) \cdot \nabla)\boldsymbol{u}_n^{*h} - ((\boldsymbol{u}_n^{*h} - \boldsymbol{u}_m^{*h}) \cdot \nabla)\boldsymbol{u}_n^{*h}$ and $((\boldsymbol{u}_n^{*h} - \boldsymbol{u}_m^{*h}) \cdot \nabla)\theta^h + ((\boldsymbol{u}^{*h} - \boldsymbol{u}_m^{*h}) \cdot \nabla)\theta_n^h - ((\boldsymbol{u}_n^{*h} - \boldsymbol{u}_m^{*h}) \cdot \nabla)\theta_n^h$ reduce to $((\boldsymbol{u}^{*h} - \boldsymbol{u}_m^{*h}) \cdot \nabla)\boldsymbol{u}^{*h}$ and $((\boldsymbol{u}^{*h} - \boldsymbol{u}_m^{*h}) \cdot \nabla)\theta^h$, respectively. The stabilization parameters (τ_m, τ_c, and τ_θ) are defined as

$$\nabla \cdot \boldsymbol{u}^* = 0, \qquad \forall \boldsymbol{x}^* \in \Omega^f(\tau), \tag{5a}$$

$$\partial_\tau \boldsymbol{u}^* + (\boldsymbol{u}^* \cdot \nabla)\boldsymbol{u}^* = -\nabla p^* + \frac{1}{Re}\nabla \cdot (\nabla \boldsymbol{u}^* + (\nabla \boldsymbol{u}^*)') - \left(\frac{Gr}{Re^2}\boldsymbol{n}_g\right)\theta, \quad \forall \boldsymbol{x}^* \in \Omega^f(\tau), \tag{5b}$$

$$\partial_\tau \theta + (\boldsymbol{u}^* \cdot \nabla)\theta = \frac{1}{RePr}\nabla^2\theta, \quad \forall \boldsymbol{x}^* \in \Omega^f(\tau), \tag{5c}$$

$$\boldsymbol{u}^* = \tilde{\boldsymbol{u}}^*; \quad \theta = \tilde{\theta}, \qquad \forall \boldsymbol{x}^* \in \Gamma_D^f(\tau), \tag{5d}$$

$$\left(-p^*\boldsymbol{I} + \frac{2}{Re}\varepsilon(\boldsymbol{u}^*)\right)\cdot\boldsymbol{n} = \tilde{\boldsymbol{h}}^*; \left(\frac{1}{RePr}\nabla\theta\right)\cdot\boldsymbol{n} = \tilde{q}^*, \quad \forall \boldsymbol{x}^* \in \Gamma_N^f(\tau), \tag{5e}$$

$$\boldsymbol{u}^* = \tilde{\boldsymbol{u}}_0^*; \quad \theta = \tilde{\theta}_0, \qquad \forall \boldsymbol{x}^* \in \Omega^f(0), \tag{5f}$$

$$\begin{aligned}
&\underbrace{\int_{\Omega^f}\left[\boldsymbol{\psi}_u^h \cdot \left(\partial_\tau \boldsymbol{u}^{*h}|_{\mathscr{X}} + \left(\left(\boldsymbol{u}_n^{*h} - \boldsymbol{u}_m^{*h}\right)\cdot\nabla\right)\boldsymbol{u}^{*h} + \left(\left(\boldsymbol{u}^{*h} - \boldsymbol{u}_m^{*h}\right)\cdot\nabla\right)\boldsymbol{u}_n^{*h} - \left(\left(\boldsymbol{u}_n^{*h} - \boldsymbol{u}_m^{*h}\right)\cdot\nabla\right)\boldsymbol{u}_n^{*h} + \left(\frac{Gr}{Re^2}\boldsymbol{n}_g\right)\theta^h\right) + \varepsilon\left(\boldsymbol{\psi}_u^h\right) : \boldsymbol{\sigma}\{\boldsymbol{u}^{*h}, p^{*h}\}\right] d\Omega}_{\mathscr{B}_G\left([\boldsymbol{\psi}_u^h, \psi_p^h], [\boldsymbol{u}^{*h}, p^{*h}, \theta^h]\right)} \\
&\underbrace{-\int_{\Gamma_N^f} \boldsymbol{\psi}_u^h \cdot \tilde{\boldsymbol{h}}^{*h}\, d\Gamma + \int_{\Omega^f}\left[\psi_p^h \nabla\cdot\boldsymbol{u}^{*h}\right] d\Omega}_{\mathscr{B}_G\left([\boldsymbol{\psi}_u^h, \psi_p^h], [\boldsymbol{u}^{*h}, p^{*h}, \theta^h]\right)} \underbrace{-\int_{\Gamma_{N(out)}^f} \boldsymbol{\psi}_u^h \cdot \left[-\frac{1}{Re}(\nabla \boldsymbol{u}^{*h})'\cdot\boldsymbol{n}\right] d\Gamma}_{\mathscr{B}_{corr}\left(\boldsymbol{\psi}_u^h, \boldsymbol{u}^{*h}\right)} + \underbrace{\sum_{e=1}^{n_{el}}\int_{\Omega^f}\tau_m\left[\left(\left(\boldsymbol{u}_n^{*h} - \boldsymbol{u}_m^{*h}\right)\cdot\nabla\right)\boldsymbol{\psi}_u^h - \frac{1}{Re}\nabla^2\boldsymbol{\psi}_u^h + \nabla\psi_p^h\right]\cdot}_{\mathscr{B}_S\left([\boldsymbol{\psi}_u^h, \psi_p^h], [\boldsymbol{u}^{*h}, p^{*h}, \theta^h]\right)} \\
&\underbrace{\left[\partial_\tau \boldsymbol{u}^{*h}|_{\mathscr{X}} + \left(\left(\boldsymbol{u}_n^{*h} - \boldsymbol{u}_m^{*h}\right)\cdot\nabla\right)\boldsymbol{u}^{*h} - \frac{1}{Re}\nabla^2\boldsymbol{u}^{*h} + \nabla p^{*h} + \left(\frac{Gr}{Re^2}\boldsymbol{n}_g\right)\theta^h\right] d\Omega + \sum_{e=1}^{n_{el}}\int_{\Omega^f}\tau_c\left[\left(\nabla\cdot\boldsymbol{\psi}_u^h\right)\left(\nabla\cdot\boldsymbol{u}^{*h}\right)\right] d\Omega}_{\mathscr{B}_S\left([\boldsymbol{\psi}_u^h, \psi_p^h], [\boldsymbol{u}^{*h}, p^{*h}, \theta^h]\right)} \\
&+ \underbrace{\int_{\Omega^f}\left[\psi_\theta^h \cdot \left(\partial_\tau \theta^h|_{\mathscr{X}} + \left(\left(\boldsymbol{u}_n^{*h} - \boldsymbol{u}_m^{*h}\right)\cdot\nabla\right)\theta^h + \left(\left(\boldsymbol{u}^{*h} - \boldsymbol{u}_m^{*h}\right)\cdot\nabla\right)\theta_n^h - \left(\left(\boldsymbol{u}_n^{*h} - \boldsymbol{u}_m^{*h}\right)\cdot\nabla\right)\theta_n^h\right) + \frac{1}{RePr}\nabla\psi_\theta^h\cdot\nabla\theta^h\right] d\Omega}_{\mathscr{B}_G\left(\psi_\theta^h, [\boldsymbol{u}^{*h}, \theta^h]\right)} \\
&+ \underbrace{\sum_{e=1}^{n_{el}}\int_{\Omega^f}\tau_\theta\left[\left(\left(\boldsymbol{u}_n^{*h} - \boldsymbol{u}_m^{*h}\right)\cdot\nabla\right)\psi_\theta^h - \frac{1}{RePr}\nabla^2\psi_\theta^h\right]}_{\mathscr{B}_S\left(\psi_\theta^h, [\boldsymbol{u}^{*h}, \theta^h]\right)} \cdot \underbrace{\left[\partial_\tau \theta^h|_{\mathscr{X}} + \left(\left(\boldsymbol{u}_n^{*h} - \boldsymbol{u}_m^{*h}\right)\cdot\nabla\right)\theta^h - \frac{1}{RePr}\nabla^2\theta^h\right] d\Omega}_{\mathscr{B}_S\left(\psi_\theta^h, [\boldsymbol{u}^{*h}, \theta^h]\right)} \underbrace{-\int_{\Gamma_N^f}\left[\psi_\theta^h \tilde{q}^{*h}\right] d\Gamma}_{\mathscr{B}_G\left(\psi_\theta^h, \theta^h\right)} = 0, \\
&\forall\left[\boldsymbol{\psi}_u^h, \psi_p^h, \psi_\theta^h\right] \in V_u^h \times V_p^h \times V_\theta^h,
\end{aligned} \tag{6}$$

Published under an exclusive license by AIP Publishing

$$\tau_m = \left[\left(\frac{2}{dt}\right)^2 + \left(\frac{2||\boldsymbol{u}^*||}{h}\right)^2 + 9\left(\frac{4}{Reh^2}\right)^2\right]^{-1/2}, \tag{7a}$$

$$\tau_c = \frac{h}{2}||\boldsymbol{u}^*||\gamma, \quad \text{for}\,\gamma = \begin{cases} Re_u/3, & 0 < Re_u \le 3, \\ 1, & 3 < Re_u, \end{cases} \tag{7b}$$

$$\tau_\theta = \left[\left(\frac{2}{dt}\right)^2 + \left(\frac{2||\boldsymbol{u}^*||}{h}\right)^2 + 9\left(\frac{4}{RePrh^2}\right)^2\right]^{-1/2}, \tag{7c}$$

where Re_u and h, respectively, are the local Reynolds number and the size of element. The value of $\boldsymbol{u}_m$ is the dimensionless mesh velocity. In Eq. (6), the Reynolds number, Prandtl number, Richardson number, and Grashof number are defined as

$$Re = \frac{U_\infty D}{\nu}; \quad Pr = \frac{\nu}{\alpha}; \quad Ri = \frac{Gr}{Re^2}; \tag{8a}$$

$$Gr = \frac{g\beta(T_H - T_C)D^3}{\nu^2}. \tag{8b}$$

The fluid solver is coupled with the structural solver by satisfying the kinematic and dynamic constraints along the fluid-structure interface (Γ^{fs}), as presented in the following equation:

$$\boldsymbol{u}^*(\boldsymbol{\Phi}^*(\mathscr{X},\tau),\tau) = \partial_\tau \boldsymbol{\Phi}^*(\mathscr{X},\tau), \quad \forall \mathscr{X} \in \Gamma^{fs}(\tau), \tag{9a}$$

$$\boldsymbol{h}^*(\boldsymbol{\Phi}^*(\mathscr{X},\tau),\tau) = -\boldsymbol{h}^{*cyl}(\boldsymbol{\Phi}^*(\mathscr{X},\tau),\tau), \quad \forall \mathscr{X} \in \Gamma^{fs}(\tau), \tag{9b}$$

where $\boldsymbol{h}^*$ and $\boldsymbol{h}^{*cyl} = [h_x^{*cyl}, h_y^{*cyl}]$, respectively, are the dimensionless fluid and structural stresses along the fluid-structure interface. The value of $\boldsymbol{\Phi}^*$ is the dimensionless location of the structure, which is defined in Eq. (10), where $\boldsymbol{\eta}^*$ is the dimensionless displacement of structure at time τ. In this investigation, the referential coordinates can be taken as the initial position of the rigid circular cylinder. The values of $\partial_\tau \boldsymbol{\Phi}^*$ and $\partial_\tau^2 \boldsymbol{\Phi}^*$ are defined as the structural velocity and acceleration, respectively,

$$\boldsymbol{\Phi}^*(\mathscr{X},\tau) = \boldsymbol{\eta}^*(\mathscr{X},\tau) + \mathscr{X}, \quad \forall \mathscr{X} \in \Omega^s(\tau). \tag{10}$$

The superscript (s) indicates the structural variables. Hence, the governing equation of the structure can be formulated as follows:

$$\begin{aligned} &\partial_\tau^2 \boldsymbol{\Phi}^* + \boldsymbol{c}\partial_\tau \boldsymbol{\Phi}^* + \boldsymbol{k}\boldsymbol{\eta}^* = \boldsymbol{h}^{*cyl}, \quad \forall \mathscr{X} \in \Omega^s(\tau), \\ &\boldsymbol{c} = 2\zeta\sqrt{\boldsymbol{k}m^s}, \quad \boldsymbol{k} = (2\pi \boldsymbol{f}_n)^2 m^s, \\ &Ur = U_\infty/(f_{ny}D), \quad m^s = m^*(0.25\pi D^2 L\rho_0), \end{aligned} \tag{11}$$

where $\boldsymbol{c} = [c_x, c_y]'$, $\boldsymbol{k} = [k_x, k_y]'$, and $\boldsymbol{f}_n = [f_{nx}, f_{ny}]'$, respectively, are the resultant damping coefficient vector, the resultant stiffness coefficient vector, and the structural frequency vector. m^* is the mass ratio and ζ is the damping ratio. The reduced velocity (Ur) is defined based on the structural frequency in the transverse direction (f_{ny}). In this investigation, it is assumed that the structural frequencies in transverse and streamwise directions are identical. The values of $D = 1.0$, $L = 1.0$ and m^s are the diameter, spanwise length, and mass of the cylinder. In the ALE description, the coordinates of mesh nodes are mapped using a popular harmonic model, whose strong form reads as

$$\begin{aligned} &-\nabla \cdot (\alpha_e \nabla \boldsymbol{d}^*) = 0, \quad \forall \boldsymbol{x}^* \in \Omega^f(\tau), \\ &\tilde{\boldsymbol{d}}^* = \boldsymbol{\eta}^*, \quad \forall \boldsymbol{x}^* \in \Gamma^{fs}(\tau), \\ &\tilde{\boldsymbol{d}}^* = \boldsymbol{0}, \quad \forall \boldsymbol{x}^* \in \Gamma^f(\tau)/\Gamma^{fs}(\tau), \end{aligned} \tag{12}$$

where $\boldsymbol{d}^*$ are the dimensionless grid displacement with respect to the fixed referential framework $\mathscr{X}$. The value of α_e is a "stiffness parameter" of the mesh.[51]

To couple the fluid and structural solvers, a second-order staggered-partitioned weakly coupling FSI scheme is implemented.[47] Both the solutions to the fluid and structural solvers march in time with the popular second-order unconditionally stable generalized α time integration schemes. For the detailed formulations of the FSI scheme and the generalized α time integration schemes, please refer to Chung and Hulbert[52] and Jansen *et al.*[53]

In many mixed convective flow applications, there are two important quantities of interest: the rate of heat convection, Nusselt number (Nu), and the hydrodynamic forces (C_d and C_l) exerted along the submerged structure and Strouhal number (St), as defined in the following equation:

$$Nu(s) = -\nabla\theta(s) \cdot \boldsymbol{n}(s); \quad Nu = \frac{1}{\ell}\int_{s=0}^{\ell} Nu(s)\, ds; \tag{13a}$$

$$C_d = \frac{h_x^{*cyl}}{0.5\rho_0 U_\infty^2 DL}; \quad C_l = \frac{h_y^{*cyl}}{0.5\rho_0 U_\infty^2 DL}; \tag{13b}$$

$$C_e = \int C_l v^* d\tau; \quad St = \frac{f_{vs}D}{U_\infty}. \tag{13c}$$

In particular, the energy transfer coefficient (C_e) in transverse direction is an important parameter in the analysis of fluid-structure interaction, which defines the total kinetic energy transferred between fluid and structure for a time interval. In this investigation, we employ these global quantities to analyze and quantify the hydrodynamic and thermal characteristics of an elastically mounted cylinder in different flow regimes.

III. PROBLEM STATEMENT AND VALIDATION

In this section, the configuration of computational domain and its hydrodynamic and thermal boundary conditions are illustrated at first. Subsequently, the mesh and time convergence analyses are conducted to determine the optimal spatial and temporal discretizations for the simulations. The implemented numerical formulations are validated with literature. The obtained numerical results match well with the benchmark examples in literature.

A. Problem setup and boundary conditions

In this investigation, the numerical investigation is conducted for the flow over a heated vibrating circular cylinder subject to cross buoyancy in mixed convective flow. As illustrated in Fig. 1(a), the cylinder is initially placed at the origin of the axes $\boldsymbol{x}^* = (0, 0)$, which is ten-diameter downstream the inlet ($L_u = 10$), forty-diameter upstream the outlet ($L_d = 40$), and twenty-five-diameter away from the upper and lower traction-free boundaries. The blockage ratio is 2%. The cylinder's diameter is taken as the characteristic length, $D = 1.0$. The rigid circular cylinder is attached with spring-damper systems and allowed to vibrate along x (streamwise) and y (transverse) axes. In this article, the Reynolds number, mass ratio, and damping ratio are fixed at $Re = 100.0$, $m^* = 10.0$, and $\zeta^* = 0.01$, respectively. The traction-free thermal and momentum boundary conditions are imposed along the boundaries of the computational domain, as shown in Fig. 1(a), except the inlet and cylinder. A uniform velocity ($\tilde{\boldsymbol{u}}^* = [U_\infty, 0.0]'$) and a

Published under an exclusive license by AIP Publishing

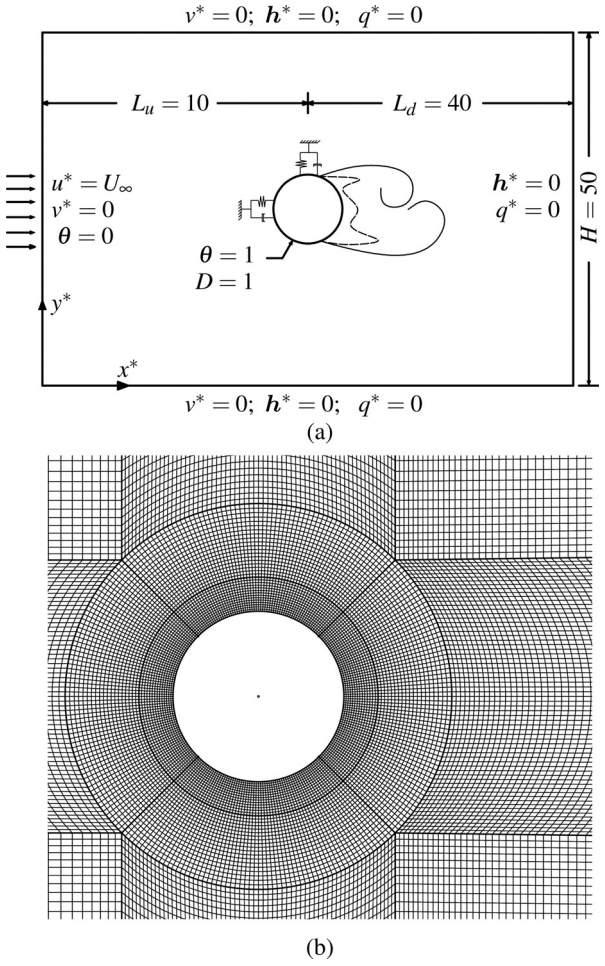

FIG. 1. Schematic diagram and mesh discretization: (a) schematic diagram of an elastically mounted cylinder in mixed convective flow and (b) mesh discretization around the wake behind the cylinder.

homogeneous temperature ($\theta = 0.0$) are imposed along the inlet. The uniform temperature ($\theta = 1.0$) is prescribed over the cylinder's surface. The instantaneous velocity and location of the cylinder are determined by the structural dynamics. The boundary-layer mesh consists of structural meshes along the cylinder's surface and grow outward (mesh growth rate less than 1.03) to avoid mesh skewness, as demonstrated in Fig. 1(b). The height of the first boundary-layer mesh is controlled well below the linear viscous sublayer $y^+ = 1.0$, where y^+ is the dimensionless wall distance. Unlike the isothermal incompressible fluid flow, the authors noticed that the height of the first boundary layer mesh should be much less than $y^+ = 1.0$ for the mixed convective flow, so as to achieve the mesh convergence, e.g., $y^+ \lesssim 0.3$.

The hydrodynamic and thermal characteristics of the vibrating cylinder are investigated in different flow regimes by varying the reduced velocity, Prandtl number, and Richardson number. The characteristic phenomena of VIV usually occur within the range of $Ur \in [2.0, 10.0]$, e.g., VIV lock-in, fluttering, and galloping. The flow of the gases and water is of our focus in this article, so the range of Prandtl number is chosen as $Pr \in [0.7, 2.0]$. For mixed convective flow, the values of Richardson number are chosen from $Ri \in [0.5, 2.0]$, where the influence of fluid inertia is more dominant over cross buoyancy.

B. Validation and convergence analysis

As illustrated in Fig. 1(b), the computational domain is discretized with four-node quadrilateral elements. The fluid velocity vector, pressure, and temperature are collocated at each node of the elements. The mesh convergence analysis is carried out for simulation of flow over a circular cylinder in mixed convective flow at $Re = 100$, $Pr = 0.8$, $Ri = 1.0$, and $dt = 0.01$. From Table I, it is evident that the error of the hydrodynamic and thermal responses is within 1% for the mesh resolution M2, where $\overline{C_d}$, C_l^{rms}, St, and $\overline{Nu}$, respectively, are the mean drag coefficient, the root mean square lift coefficient, Strouhal number, and the mean Nusselt number. Hence, M2 is used for all simulations in this article. The value in the bracket of the column of "MESH" refers to the number of nodes around the cylinder. The results of time convergence analysis together with the approximated maximum Courant–Friedrichs–Lewy (CFL) numbers are listed in Table II. Since the unconditionally stable second order accurate generalized α time integration is used for fluid formulation, the restriction of critical CFL number is less stringent than the other explicit time integration schemes in order to satisfy the stability requirement. In terms of accuracy, the time convergence analysis in Table II shows that the time step $dt = 0.01$ is optimal for the investigation of mixed convective flow, where the errors of the hydrodynamic and thermal responses are within 1% compared with the referential values at $dt = 0.005$.

Subsequently, the derived numerical formulation is validated with the results in literature. It can be seen that the obtained mean Nusselt numbers from the derived formulation for heat convection flow match well with the literature[13,54] and the empirical formula[55] in Eq. (14), as shown in Fig. 2(a),

$$\overline{Nu} = 0.3 + \frac{0.62 Re^{1/2} Pr^{1/3}}{\left[1 + (0.4/Pr)^{2/3}\right]^{1/4}} \left[1 + \left(\frac{Re}{282000}\right)^{5/8}\right]^{4/5}. \quad (14)$$

TABLE I. Flow past a circular cylinder in mixed convective flow at $Re = 100$, $Pr = 0.7$, $Ri = 1.0$, $dt = 0.01$ and different mesh resolutions.

MESH	NODES	$\overline{C_d}$	C_l^{rms}	St	$\overline{Nu}$
M3 (128)	2.6×10^4	1.300 (0.5%)	0.251 (1.9%)	0.175 (0.0%)	5.106 (1.8%)
M2 (256)	4.8×10^4	1.306 (0.0%)	0.255 (0.4%)	0.175 (0.0%)	5.191 (0.2%)
M1 (512)	8.9×10^4	1.306	0.256	0.175	5.198

Published under an exclusive license by AIP Publishing

TABLE II. Flow past a circular cylinder in mixed convective flow at $Re = 100$, $Pr = 0.7$, $Ri = 1.0$, M2 (256) and different time steps.

TIME STEP	$\overline{C_d}$	C_l^{rms}	St	$\overline{Nu}$	Max CFL
$dt = 0.020$	1.287 (1.5%)	0.236 (8.0%)	0.175 (0.0%)	5.096 (2.2%)	1.87
$dt = 0.010$	1.306 (0.0%)	0.255 (0.8%)	0.175 (0.0%)	5.191 (0.4%)	0.92
$dt = 0.005$	1.307	0.257	0.175	5.211	0.45

The derived formulation for the unsteady, incompressible, and isothermal fluid flow is validated with literature[56,57] by comparing the hydrodynamic forces in Fig. 2(b). The structural dynamics obtained from the implemented ALE formulation is validated by comparing the values of the dimensionless transverse fluctuation in literature.[58–60] The maximum values of a dimensionless quantity are defined based on its root mean square and mean values. For instance,

$$A_y^{\max} = \delta A_y^{\max} + \overline{A_y}, \quad \delta A_y^{\max} = \sqrt{2} A_y^{rms}, \tag{15a}$$

$$A_y^{rms} = \sqrt{\frac{\sum_i^n \left(A_y(i) - \overline{A_y}\right)^2}{n}}, \tag{15b}$$

where A^{max}, $\delta A_y^{\max}$, A_y^{rms}, and $\overline{A_y}$ are the maximum transverse displacement, the maximum transverse fluctuation, the root mean square (rms) transverse fluctuation, and the mean transverse displacement of the cylinder, respectively. The value of n is the total number of sampled data. The same formula is used to compute the maximum, the

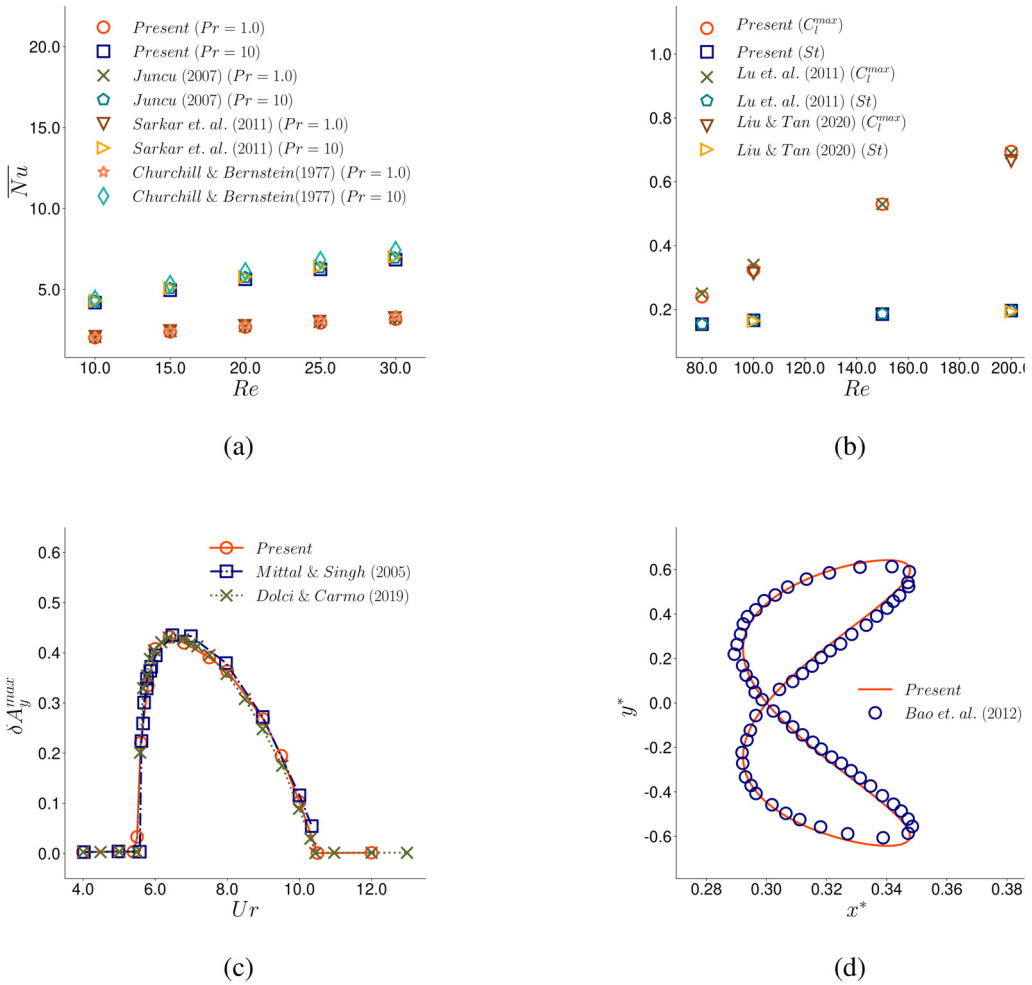

FIG. 2. Validation of the implemented numerical algorithm: (a) flow past a circular cylinder in forced convection flow; (b) flow past a circular cylinder in isothermal fluid flow; (c) flow past an elastically mounted cylinder at $Re = 33$, $m^* = 4.73$, and $\zeta = 0$, and (d) flow pas an elastically mounted cylinder at $Re = 150$, $m^* = 2.55$, $\zeta = 0$, and $Ur = 5.0$.

Published under an exclusive license by AIP Publishing

rms, and mean values of C_d, C_l, and Nu too. Figure 2(c) shows the good agreement of the VIV lock-in responses with literature. Figure 2(d) demonstrates the typical figure-eight trajectory obtained from the derived numerical formulation for the freely vibrating cylinder in the isothermal cross flow.

IV. RESULTS AND DISCUSSION

In mixed convective flow, thermal buoyancy effect is non-negligible in the flow. It influences hydrodynamic stability in wake due to strong temperature gradient next to the heated cylinder's surface. The thermal energy rapidly diffuses downstream and perturbs shear-layer interaction in wake. The powerful influence of cross buoyancy results in complicated hydrodynamic and structural responses compared with isothermal flow. In mixed convective flow, the influence of heat convection is frequently defined by two parameters, Prandtl (Pr) and Richardson numbers (Ri). Prandtl number defines how diffusive the heat energy is with respect to fluid momentum. On the other hand, Richardson number represents the importance of buoyancy action over fluid inertia, which is also a key indicator how significant the natural convection is in mixed convective flow. In this section, we focus on the study on the subtle interactions between fluid, structure, and cross thermal buoyancy for different Prandtl and Richardson numbers, e.g., $Pr \in [0.7, 10]$ and $Ri \in [0.5, 2.0]$.

A. Structural dynamics and secondary VIV lock-in

Cross buoyancy effects boundary layer dynamics around structure and shear-layer interaction in wake along gravitational direction because of the presence of strong temperature gradient. It results in drastic changes in hydrodynamic forces and the associated structural dynamics. For instance, Fig. 3 exhibits the cases of $Re = 30$ and $Pr = 0.7$ before the onset of vortex shedding. Due to cross thermal buoyancy, strong asymmetry of boundary layer separation and thicknesses are found around the cylinder's surface. Figure 3(a) shows that there are two symmetric separation points of boundary layer appearing at approximately 132° on both sides of the cylinder in forced convection condition. In contrast, Fig. 3(b) shows the boundary layers asymmetrically separate at multiple locations and form laminar separation bubble along the cylinder's surface in the case of mixed convection ($Pr = 0.7$ and $Ri = 2.0$). These differences in boundary layer separation and reattachment of shear layers indicate phenomenal changes in hydrodynamic forces caused by cross buoyancy. The similar trend are also observed in the cases of $Re = 100$ after the onset of vortex shedding in mixed convection. These changes of hydrodynamic forces are quantified by computing the deviation of mean value of lift coefficient ($\overline{C_l}$) for the cases of $Re = 100$, $Pr \in [0.7, 10.0]$, and $Ri \in [0.0, 2.0]$ in Fig. 4. It is found the higher values of $\overline{C_l}$ appears in cases of small Prandtl numbers and larger Richardson numbers, which signifies a strong buoyancy action exerted in transverse direction. Furthermore, in the cases of a vibrating cylinder, the vortex dynamics is expected to be much more complicated and requires thorough analysis over other key parameters. The detailed discussion will be elaborated carefully in the rest of this article.

To compare structural dynamics in isothermal and mixed convective flow, the analysis starts from streamwise motions of a freely vibrating circular cylinder. Figure 5 shows that the changes of mean streamwise displacement ($\overline{A_x}$) with respect to reduced velocity (Ur) is

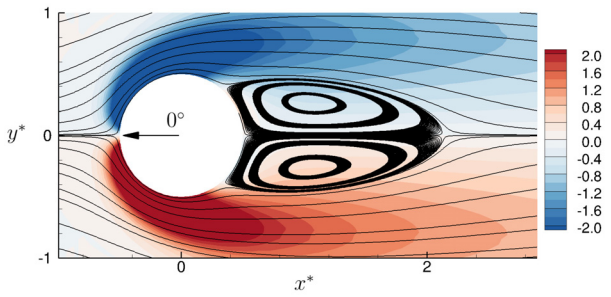

(a) $Ri = 0.0$

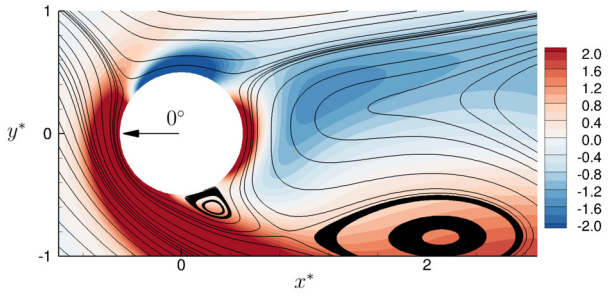

(b) $Ri = 2.0$

FIG. 3. Boundary layer separation point around a stationary heated cylinder at $Re = 30$, $Pr = 0.7$, $Ri = [0.0, 2.0]$, and $\tau = 350.0$: (a) separation point = 132° for $Ri = 0.0$ (forced convection) and (b) separation point = 134° and 92° for $Ri = 2.0$ (mixed convection). The angle is measured from the leading edge of cylinder. The contours are colored by spanwise vorticity $\omega \in [-2.0, 2.0]$.

insensitive to changes of Pr and Ri values, except for a relative augmentation of amplitude (about 40%) during VIV lock-in. The values of $\overline{A_x}$ grow proportionally with Ur values. On the contrary, the maximum streamwise fluctuations ($\delta A_x^{\max}$) exhibit drastic changes in cases of different Pr and Ri values. In the cases in mixed convection subject

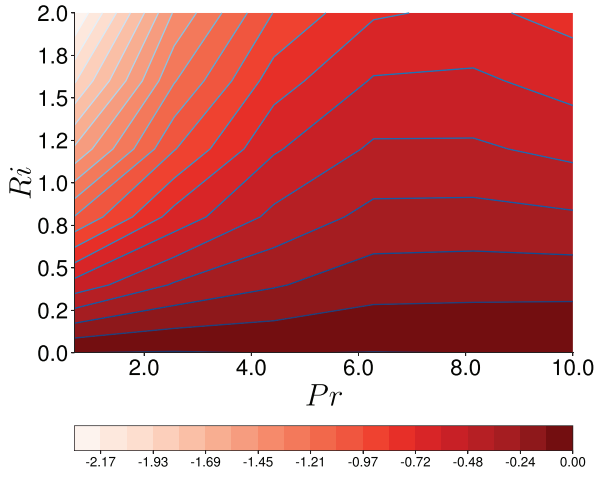

FIG. 4. Deviation of the mean value of lift coefficient ($\overline{C_l}$) of a circular cylinder in mixed convective flow for $Re = 100$, $Pr \in [0.7, 10.0]$ and $Ri \in [0.0, 2.0]$.

Published under an exclusive license by AIP Publishing

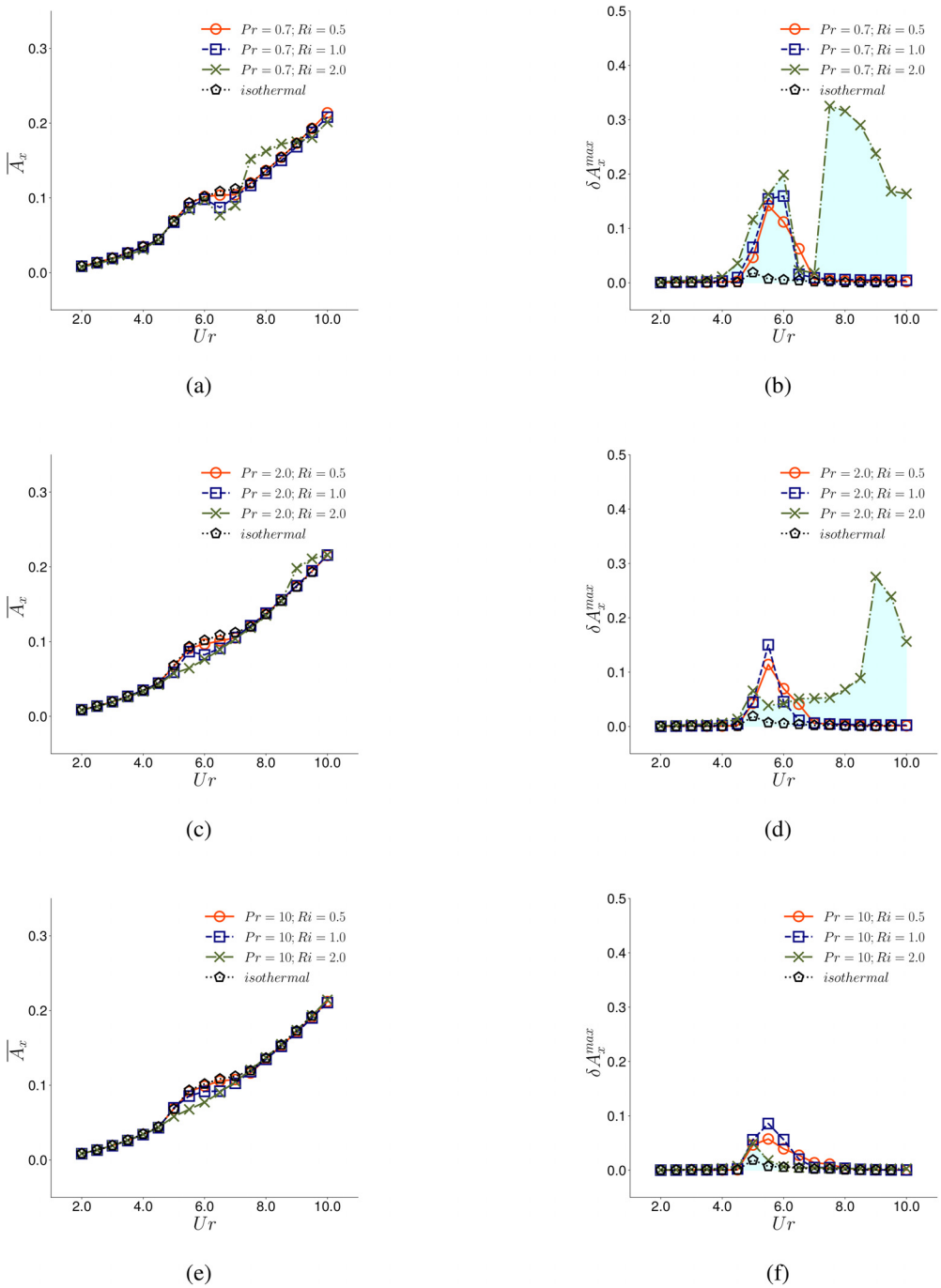

FIG. 5. Streamwise structural dynamics of a freely vibrating cylinder at $Re = 100$, $m^* = 10$, $\zeta = 0.01$, $Ur \in [2, 10]$, $Pr \in [0.7, 10]$, and $Ri \in [0.5, 2.0]$: (a), (c), and (e) the mean streamwise displacement and (b), (d), and (f) the maximum streamwise fluctuation. The VIV lock-in regions for $Ri = 2.0$ are filled with *light cyan* color.

to cross thermal buoyancy, the values of $\delta A_x^{\max}$ are significantly amplified during VIV lock-in compared with those in isothermal flow. However, as Prandtl number grows further, e.g., $Pr = 10.0$ in Fig. 5(f), this difference gets minimized. It implies that the slower dissipation of heat energy with respect to fluid momentum (higher Prandtl number) limits its influence on hydrodynamic forces. This conclusion is going to be supported further by the subsequent analyses of transverse structural vibration (A_y) and numerical results in Secs. IV B and IV C.

Published under an exclusive license by AIP Publishing

In addition, it can be observed in Figs. 5(b), 5(d), and 5(f) that VIV lock-in is further extended to much higher reduced velocity values ($Ur \approx 10$) in the cases of $Ri = 2.0$. In particular, Fig. 5(b) obviously shows a secondary VIV lock-in occurring over $Ur \in (7.0, 10)$ in the case of $Pr = 0.7$ and $Ri = 2.0$. This secondary VIV lock-in implies a strong influence of cross buoyancy on structural dynamics for high Ur values. In addition, the structural vibration is also found insensitive to cross buoyancy during the pre-lock-in. Again, Fig. 5(d) shows an

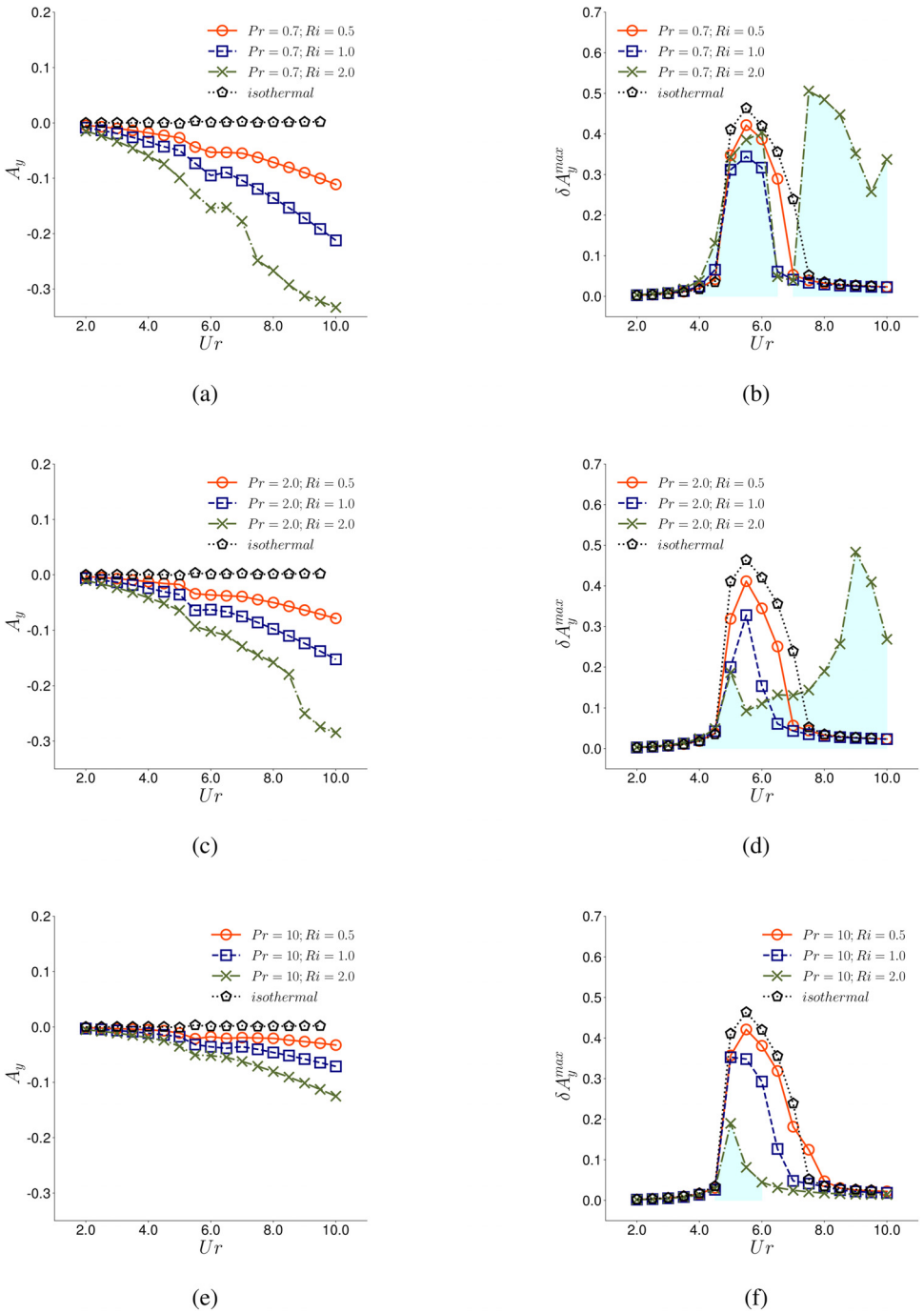

FIG. 6. Transverse structural dynamics of a freely vibrating cylinder at $Re = 100$, $m^* = 10$, $\zeta = 0.01$, $Ur \in [2, 10]$, $Pr \in [0.7, 10]$, and $Ri \in [0.5, 2.0]$: (a), (c), and (e) the mean transverse displacement and (b), (d), and (f) the maximum transverse fluctuation. The VIV lock-in regions for $Ri = 2.0$ are filled with *light cyan* color.

Published under an exclusive license by AIP Publishing

extended VIV lock-in formed by coalescence of the primary and secondary VIV lock-in in the case of $Pr = 2.0$ and $Ri = 2.0$, the dotted green curve with *cross* markers. However, in the case of high Prandtl and Richardson numbers, e.g., $Pr > 2.0$ and $Ri = 2.0$, the VIV lock-in becomes significantly suppressed until $Ur < 10$ instead.

Similar to the analysis of streamwise vibration, the transverse motion is plotted in Fig. 6. Unlike the streamwise displacements, the difference of mean transverse displacement ($\bar{A}_y$) between mixed convective and isothermal flow is evidently enlarged as the reduced velocity value increases in Figs. 6(a), 6(c), and 6(e). Especially, this difference becomes the largest in the cases of $Ri = 2.0$ over the same range of Ur value. Nevertheless, similar to the trend in maximum streamwise fluctuation ($\delta A_x^{\max}$), the cross buoyancy effect on hydrodynamics during VIV lock-in reduces in the cases of larger Prandtl numbers. As Prandtl number spikes, the streamwise and transverse motions become further close to those in isothermal flow, except for the cases of large Richardson numbers for high Ur values. The aforementioned secondary VIV lock-in is also confirmed in the analysis of transverse motions for $Ur \gtrsim 7.0$ in Figs. 6(b) and 6(d). The maximum transverse fluctuation ($\delta A_y^{\max}$) becomes remarkably amplified for $Ur \approx 5.5$ and $Ur \approx 9.0$, respectively. The primary and secondary VIV lock-in coalesce in the case of $Pr = 2.0$ and $Ri = 2.0$, stretching over a wide range of Ur values in Fig. 6(d). It is also noteworthy that the peak value of the secondary VIV lock-in is shifted to much higher reduced velocity values until $Ur \approx 9.25$ in this study, and the peak transverse fluctuation during the primary VIV lock-in is simultaneously suppressed, e.g., $\delta A_y^{\max} \approx 0.2$ at $Ur = 5$ in Fig. 6(d). This shift of peak value in secondary VIV lock-in is further confirmed in the subsequent analyses of hydrodynamic forces in Sec. IV B and the energy transfer in Sec. IV C. If both Prandtl and Richardson numbers are high enough, e.g., the dotted green curve with *cross* markers in Fig. 6(f), the secondary VIV lock-in could become suppressed instead over $Ur \in [2.0, 10]$, and the peak transverse fluctuation during primary VIV lock-in subsides remarkably. In a nutshell, the hydrodynamics and structural dynamics in the cases of large Pr and small Ri values become very close to those in isothermal flow. In contrast, for large Ri values, e.g., $Ri \approx 2.0$ in this study, a secondary VIV lock-in can be initiated and shift its location with respect to the Ur values for different Pr numbers. It is found that the cross thermal buoyancy has a severe impact on structural dynamics, especially over high reduced velocity values.

It is well known the frequency synchronization is a crucial behavior of VIV lock-in in the case of isothermal flow over a cylinder, which is normally observed if the vortex shedding frequency (f_{A_y}) is close to the natural frequency of structure (f_{ny}). By plotting the frequency ratio (f_{A_y}/f_{ny}), the VIV lock-in for isothermal flow could be distinguished evidently, e.g., the dotted black line with *pentagon* markers in Fig. 7(a) over $Ur \in [5.0, 7.0]$. Subject to cross buoyancy, the primary VIV lock-in becomes narrower for $Pr = 0.7$ and $Ri = [0.5, 2.0]$. Furthermore, the primary VIV lock-in becomes even more narrow in the case of $Ri = 2.0$. Similar to the primary VIV lock-in, the secondary VIV lock-in is also associated with frequency synchronization between hydrodynamic force and structural vibration. Because of the upward force induced by cross buoyancy in wake, the frequency and amplitude of hydrodynamic forces exerted on a vibrating cylinder are continuously modulated and result in further frequency synchronization for higher reduced velocity values. Consequently, the aforementioned secondary

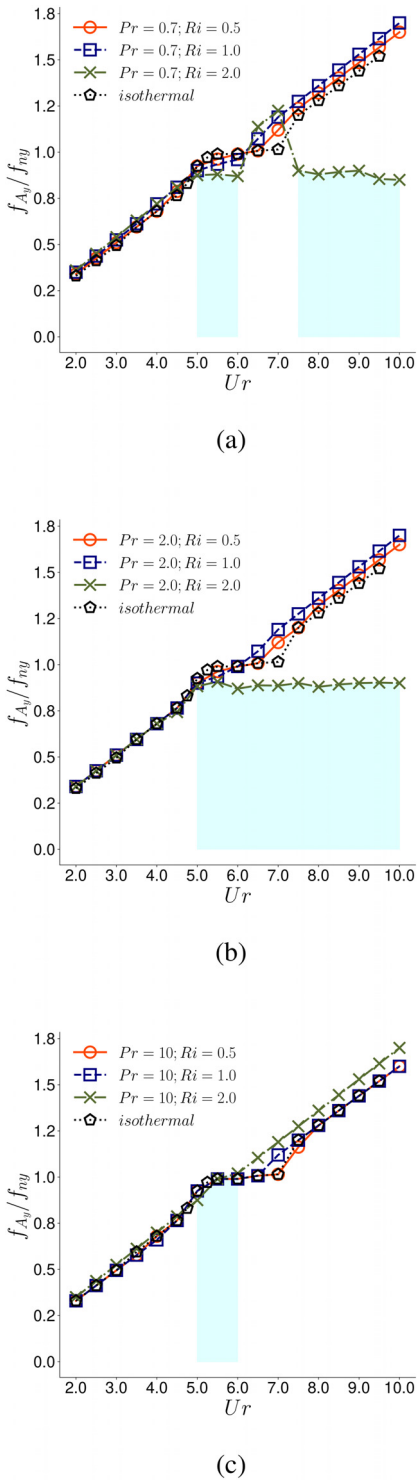

FIG. 7. Frequency ratio of a freely vibrating cylinder at $Re = 100$, $m^* = 10$, $\zeta = 0.01$, and $Ur \in [2, 10]$: (a) $Pr = 0.7$ and $Ri \in [0.5, 2.0]$; (b) $Pr = 2.0$ and $Ri \in [0.5, 2.0]$ and (c) $Pr = 10$ and $Ri \in [0.5, 2.0]$. The VIV lock-in regions for $Ri = 2.0$ are filled with *light cyan* color.

Published under an exclusive license by AIP Publishing

VIV lock-in-state is clearly confirmed again in the case of $Pr = 0.7$ and $Ri = 2.0$ for $Ur = [7.5, 10]$, the region filled by *light cyan* color in Fig. 7(a). For large Prandtl numbers, e.g., $Pr = 2.0$, the coalescence of primary and secondary VIV lock-in is confirmed again in the frequency domain, as illustrated by the *light cyan* region for $Ur > 5.0$ in Fig. 7(b). This observation is extremely meaningful for the structural dynamics, since VIV lock-in is an indicator of intensive vibrations and kinetic energy transfer between the fluid and structure. It means that the cross buoyancy effect is intense and detrimental to structural stability in the cases of small Pr and large Ri values. Analogous to the observations in Figs. 5 and 6, the hydrodynamic and structural responses of a freely vibrating cylinder become more close to those in isothermal flow in the cases of large Pr and small Ri values instead. The frequency ratios for $Ri = 0.5$ and 1.0, as plotted in Fig. 7(c), behave almost identical to the responses in isothermal flow, except for the case of $Ri = 2.0$, where the VIV lock-in is severely suppressed.

As shown in Fig. 8, the wake behind a heated vibrating cylinder is apparently deflected upward as Richardson number increases. The intensive and complicated shear-layer interaction is observed in the upper portion of wake. The temperature contour closely follows the evolution of vorticity clusters and its intensity dissipates gradually downstream. In the cases of small Ri values, e.g., Figs. 8(a) and 8(b), the strength of heat energy can sustain much farther downstream because the fluid inertia is dominant over the dynamics of heat dissipation. As Prandtl number increases until $Pr = 2.0$, the size of temperature contour becomes more concentrated at the vortex cores in Fig. 9. Similar to the cases of $Pr = 0.7$, the wake deflects upward as Richardson number keeps increasing. Furthermore, it is also found

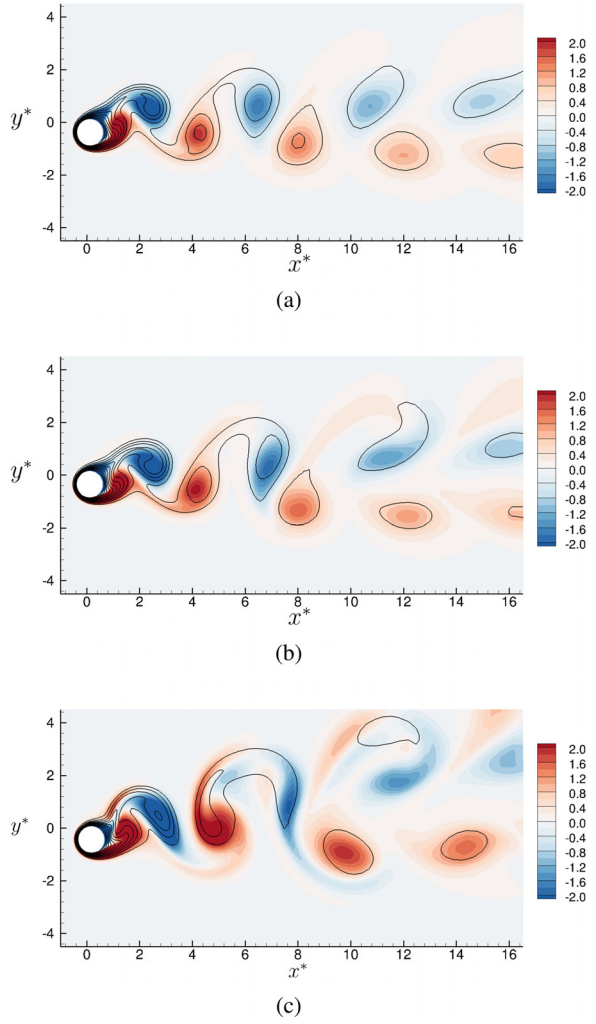

FIG. 8. Spanwise vorticity ω contour of a freely vibrating cylinder at $Re = 100$, $Pr = 0.7$, $m^* = 10$, $\zeta = 0.01$, and $Ur = 5.0$: (a) $Ri = 0.5$ and $\tau = 354.52$; (b) $Ri = 1.0$ and $\tau = 352.52$; (c) $Ri = 2.0$ and $\tau = 350.01$. The solid lines are heat energy field for $\theta \in [0.08, 0.9]$.

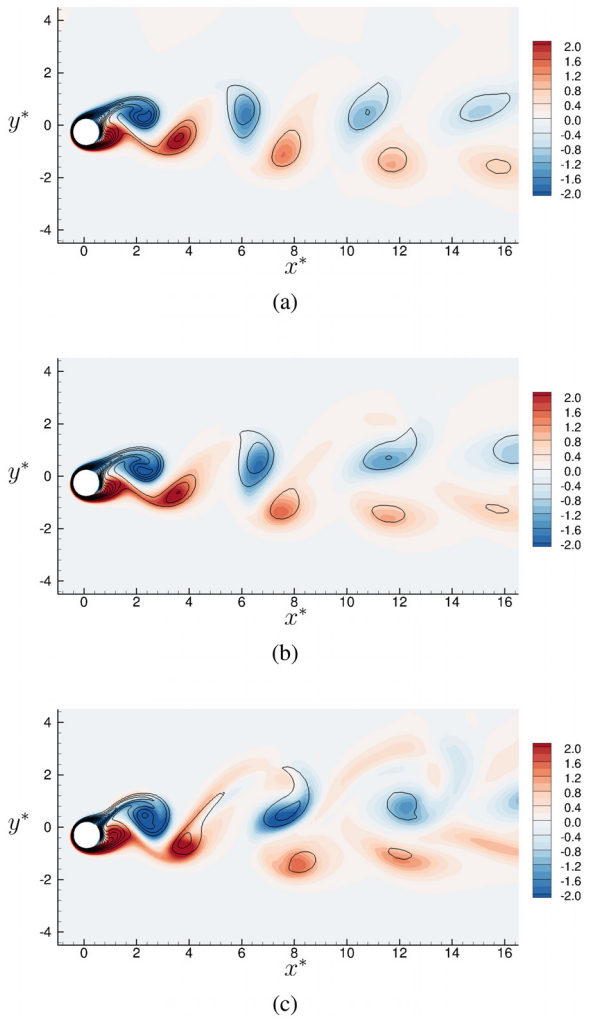

FIG. 9. Spanwise vorticity ω contour of a freely vibrating cylinder at $Re = 100$, $Pr = 2.0$, $m^* = 10$, $\zeta = 0.01$, and $Ur = 5.0$: (a) $Ri = 0.5$ and $\tau = 352.52$; (b) $Ri = 1.0$ and $\tau = 355.02$; (c) $Ri = 2.0$ and $\tau = 353.02$. The solid lines are heat energy field for $\theta \in [0.08, 0.9]$.

Published under an exclusive license by AIP Publishing

that the temperature gradient, the concentration of temperature contours, becomes stronger in the near wake right behind the cylinder, as shown in Fig. 9.

For the cases of $Pr = 10$ in Fig. 10, the temperature contour becomes further concentrated at vortex core and dissipates rapidly downstream. Since fluid inertia is dominant, the vortex dynamics in wake is very similar to those in isothermal flow, compared with the cases of smaller Pr values in Figs. 8 and 9. The downstream heat dissipation is apparently driven by the evolution of vorticity clusters. Recollecting the aforementioned discussions, it is realized the cross thermal buoyancy effect has a direct impact on hydrodynamic forces and structural dynamics due to strong temperature gradients next to the cylinder's surface. Hence, we zoom in and focus on the temperature contours around the cylinder's surface and its near wake during VIV lock-in $Ur = 5.0$. Comparing Figs. 8 and 11, it can be noticed that the dynamics of temperature contour is driven by vortex shedding in wake. A stronger cluster of temperature contour concentrates at the core of voriticity clusters. As Richardson number increases (cross buoyancy effect spikes), the temperature contour is further stretched

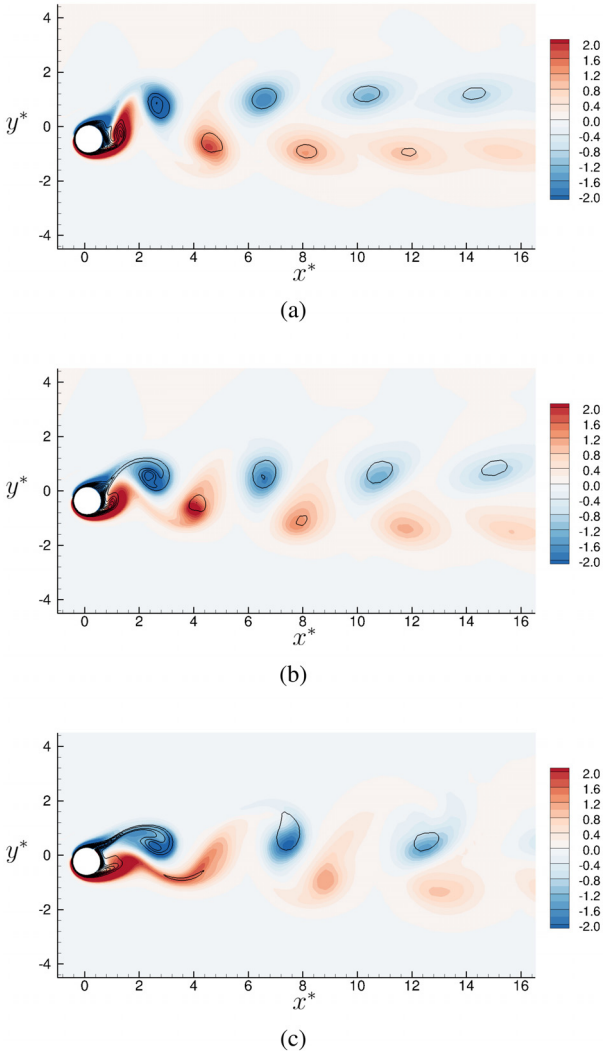

FIG. 10. Spanwise vorticity ω contour of a freely vibrating cylinder at $Re = 100$, $Pr = 10$, $m^* = 10$, $\zeta = 0.01$, and $Ur = 5.0$: (a) $Ri = 0.5$ and $\tau = 355.52$; (b) $Ri = 1.0$ and $\tau = 353.02$; (c) $Ri = 2.0$ and $\tau = 351.02$. The solid lines are temperature field for $\theta \in [0.08, 0.9]$.

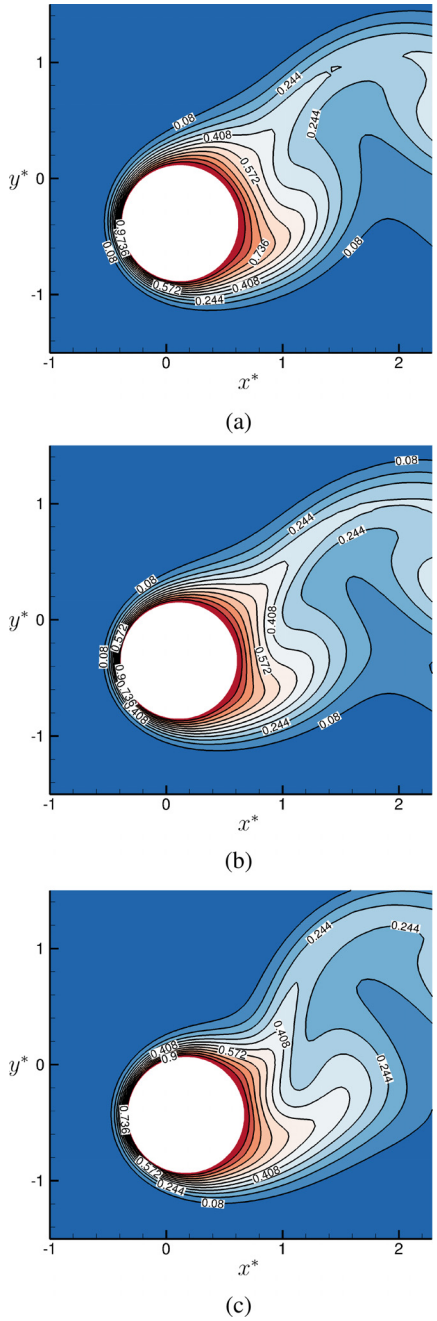

FIG. 11. Thermal contour of a freely vibrating cylinder at $Re = 100$, $Pr = 0.7$, $m^* = 10$, $\zeta = 0.01$, and $Ur = 5.0$: (a) $Ri = 0.5$ and $\tau = 354.52$; (b) $Ri = 1.0$ and $\tau = 352.52$; (c) $Ri = 2.0$ and $\tau = 350.01$.

Published under an exclusive license by AIP Publishing

in wake, e.g., Figs. 11(c), 12(c), and 13(c), and deflected upward along gravitational direction. Furthermore, due to the rapid vibration of cylinder in fluid, the temperature contour becomes extremely concentrated over the frontal area of cylinder, toward where it is rapidly moving, e.g., the upper and lower surfaces in Figs. 11(a) and 11(c), respectively. As Prandtl number increases, Fig. 12 shows that the temperature contours becomes more concentrated around the vortex cores in wake and cylinder's surface, where temperature gradient is

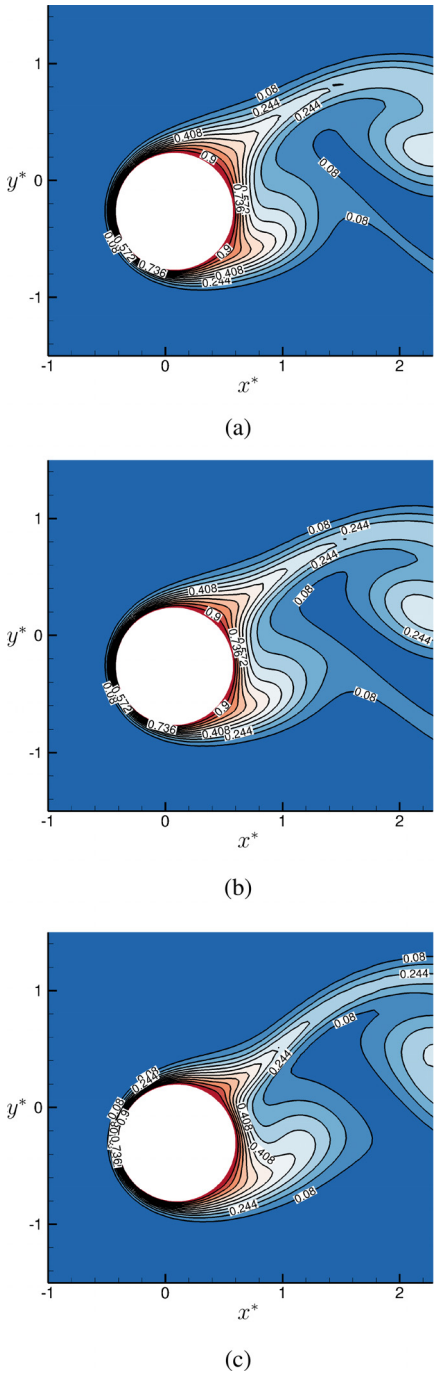

FIG. 12. Thermal contour of a freely vibrating cylinder at $Re = 100$, $Pr = 2.0$, $m^* = 10$, $\zeta = 0.01$, and $Ur = 5.0$: (a) $Ri = 0.5$ and $\tau = 352.52$; (b) $Ri = 1.0$ and $\tau = 355.02$; (c) $Ri = 2.0$ and $\tau = 353.02$.

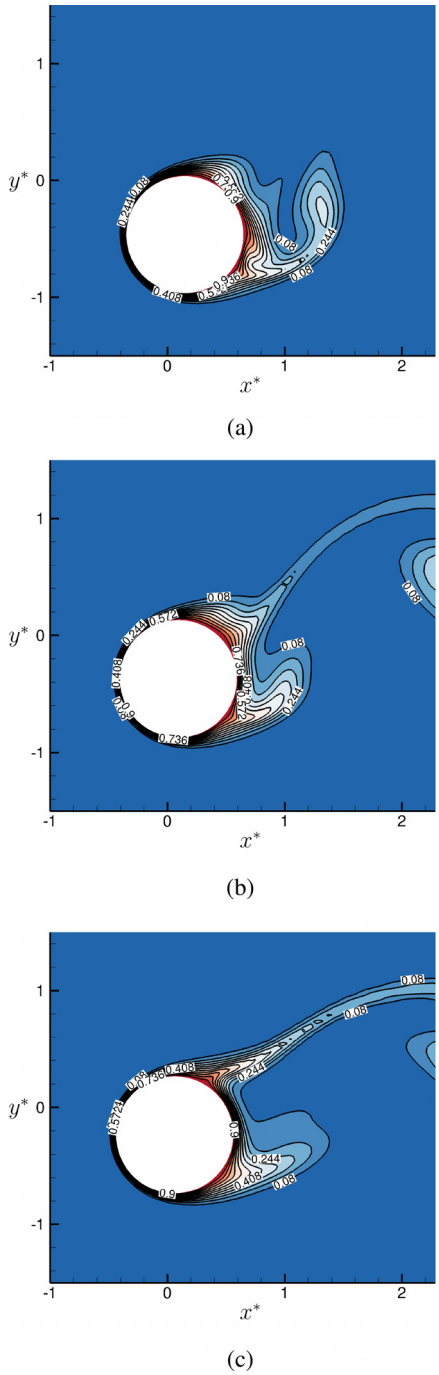

FIG. 13. Thermal contour of a freely vibrating cylinder at $Re = 100$, $Pr = 10$, $m^* = 10$, $\zeta = 0.01$, and $Ur = 5.0$: (a) $Ri = 0.5$ and $\tau = 355.52$; (b) $Ri = 1.0$ and $\tau = 353.02$; (c) $Ri = 2.0$ and $\tau = 351.02$.

Published under an exclusive license by AIP Publishing

high. It results in rapid heat convection over a cylinder's surface, which will be subsequently discussed in detail in Sec. IV C. Again, the highly concentrated temperature contour is also noticed around the cylinder's frontal surface during its drastic vibration. The detailed discussion about the characteristics of heat convection will be furnished in Sec. IV C. In cases of $Pr = 10$, the temperature contour retains highly concentrated around the entire surface of cylinder for different Ri values in Fig. 13.

B. Hydrodynamic forces of a vibrating cylinder subject to cross buoyancy

It was reported in literature that a balanced state is achieved between hydrodynamic forces and structural dynamics during the self-limiting VIV lock-in. In mixed convective flow, the cross thermal buoyancy induces upward fluid flux in transverse direction. It perturbs the balance of forces and elevates the complexity of shear-layer interaction in wake. As illustrated by the dotted black line with *pentagon* markers in Fig. 14(a), the mean drag coefficient ($\overline{C_d}$) around a vibrating cylinder in isothermal flow is about 1.32 over a wide range of Ur values, except for VIV lock-in. In contrast, for mixed convection, as Richardson number increases, the peak value of $\overline{C_d}$ during VIV lock-in reduces significantly. In cases of relatively low Richardson numbers ($Ri < 2.0$ in this study) in Figs. 14(a), 14(c), and 14(e), the values of $\overline{C_d}$ become clearly insensitive to the values of Ur, Pr, and Ri during the off lock-in states. Here, the off lock-in-state refers to the ranges of Ur values outside VIV lock-in-state, e.g., the pre- and post-VIV lock-in. On the contrary, an obvious interference of buoyancy effect happens in the cases of $Ri = 2.0$. In the case of $Pr = 0.7$ and $Ri = 2.0$ in Fig. 14(a), the value of $\overline{C_d}$ gets excited during the secondary VIV lock-in ($Ur = [7.0, 9.5]$) and becomes approximately 1.18 for the off lock-in states. The increment of Prandtl number remarkably weakens the influence of heat energy on $\overline{C_d}$ for off lock-in states in Figs. 14(a), 14(c), and 14(e).

Similar to the observation of $\overline{C_d}$, the maximum fluctuations of drag coefficient ($\delta C_d^{\max}$) are close to those of isothermal flow in the cases of $Ri < 2.0$ for $Ur \in [0.0, 10]$ in this study. Nonetheless, the diminished peak values of $\delta C_d^{\max}$ during VIV lock-in can still be clearly identified in the cases of mixed convection in Figs. 14(b), 14(d), and 14(f). Again, the secondary VIV lock-in is recorded in the cases of $Ri = 2.0$ in Figs. 14(b) and 14(d), within which the values of $\delta C_d^{\max}$ are excited significantly and become comparable to the peak values in primary VIV lock-in. Figure 14(f) also confirms that the VIV lock-in is impressively suppressed in the cases of high Prandtl ($Pr = 10.0$) and Richardson numbers ($Ri = 2.0$).

Cross thermal buoyancy causes changes of local fluid density. As result, the vortex dynamics in wake is strongly perturbed by the induced upward fluid flux opposite to the gravity. It is expected the hydrodynamic forces exerted on structure are changed correspondingly in the cases of large Ri values because of strong buoyancy action. Indeed, Figs. 15(a), 15(c), and 15(e) exhibit obvious deviations of mean lift forces ($\overline{C_l}$) over a wide range of Ur values. The magnitude of $\overline{C_l}$ spikes proportionally with Richardson number. On the contrary, the values of $\overline{C_l}$ become very close to those in isothermal flow in the cases of large Pr values in Fig. 15(e), except for the case of $Ri = 2.0$. In isothermal and incompressible fluid flow, the mean lift force around a vibrating cylinder is practically zero and indicates a balanced fluctuation state of hydrodynamic forces. However, because of the presence of cross buoyancy in mixed convection, the values of $\overline{C_l}$ become significantly excited during VIV lock-in, and its peak value becomes amplified as the value of Ri increases. Similarly, a peak value of $\overline{C_l}$ is observed during the secondary VIV lock-in for $Ur \in [8.0, 10]$ in the cases of $Pr < 10$ and $Ri = 2.0$, as shown in Figs. 15(a) and 15(c).

Compared with the value of $\overline{C_l}$, the magnitude of maximum fluctuation ($\delta C_l^{\max}$) is of a primary concern in the analyses of structural and hydrodynamic stability. In Figs. 15(b), 15(d), and 15(f), similar to those in isothermal flow, the value of $\delta C_l^{\max}$ is excited during VIV lock-in and retains a very low value during the off lock-in states, especially the post-VIV lock-in. Furthermore, it is found that the change of Prandtl number has no significant impact on the value of $\delta C_l^{\max}$ over $Ur \in [0.0, 10]$, regardless of VIV lock-in or off lock-in states. Except for the cases of $Ri = 2.0$, the values of $\delta C_l^{\max}$ for different Pr and Ri values are very close to those in isothermal fluid flow. Nonetheless, the values of $\delta C_l^{\max}$ are apparently amplified in cases of $Ri = 2.0$ in Figs. 15(b) and 15(d) over $Ur \gtrsim 7.0$ during the secondary VIV lock-in, except for the case of $Pr = 10$ and $Ri = 2.0$ in Fig. 15(f).

C. Kinetic and heat energy transfer of a vibrating cylinder subject to cross buoyancy

Based on the analyses in Secs. IV A and IV B, it is found that the heat energy has a phenomenal influence on structural dynamics and hydrodynamics in wake, especially for relatively high reduced velocity values. This observation is crucial to the subsequent discussion of energy transfer in this section. It was reported that the kinetic energy transfer between fluid and structure is inhibited during pre- and post-lock-in states in isothermal flow.[46] The appearance of secondary VIV lock-in-state for high Ur values means that the fluid kinetic energy is further transferred from fluid into structural motion subject to cross buoyancy over a wide range of Ur values, especially $Ur \gtrsim 7.0$ (the typical post-VIV lock-in-state in isothermal flow). This expectation is affirmatively supported by the results in Fig. 16, which shows the kinetic energy transfer between the fluid and structure in transverse direction for $\tau \in [200, 400]$. More than 30 cycles of vortex shedding are plotted with respect to the reduced velocity values. It can be seen that a significant amount of fluid kinetic energy is transferred into the structure in the case of $Pr = 0.7$ and $Ri = 2.0$ for high reduced velocity values, $Ur \in [7.0, 9.0]$, in Fig. 16(a), besides the primary VIV lock-in. The kinetic energy transfer is excited at almost the same Ur value for both mixed convection and isothermal flow, e.g., $Ur \approx 5.25$. However, the amount of transferred fluid kinetic energy is significantly reduced in the cases of higher Richardson numbers. Especially, it is noticed that the fluid kinetic energy transfer is almost suppressed in the cases of large Prandtl and Richardson numbers, e.g., the green dotted line with *cross* markers in Figs. 16(b) and 16(c). This finding is extremely meaningful to scientists in the research of hydropower energy harvesting for further investigations.

On the other hand, the phase angle difference is another important indicator of energy transfer. It is used to check whether a signal provides positive feedback to one another. In this study, the instantaneous phase angle difference (ϕ) between A_y and C_l is approximated by Hilbert–Huang Transform (HHT)[26,61] and averaged over $\tau = [200, 400]$. Liu and Jaiman[46] reported that the maximum energy transfer between fluid and structure occurs for $\phi \approx 90°$, in which the cylinder can obtain the maximum acceleration from the fluid force. Based on the results in Fig. 17, overall, it is confirmed that maximum

Published under an exclusive license by AIP Publishing

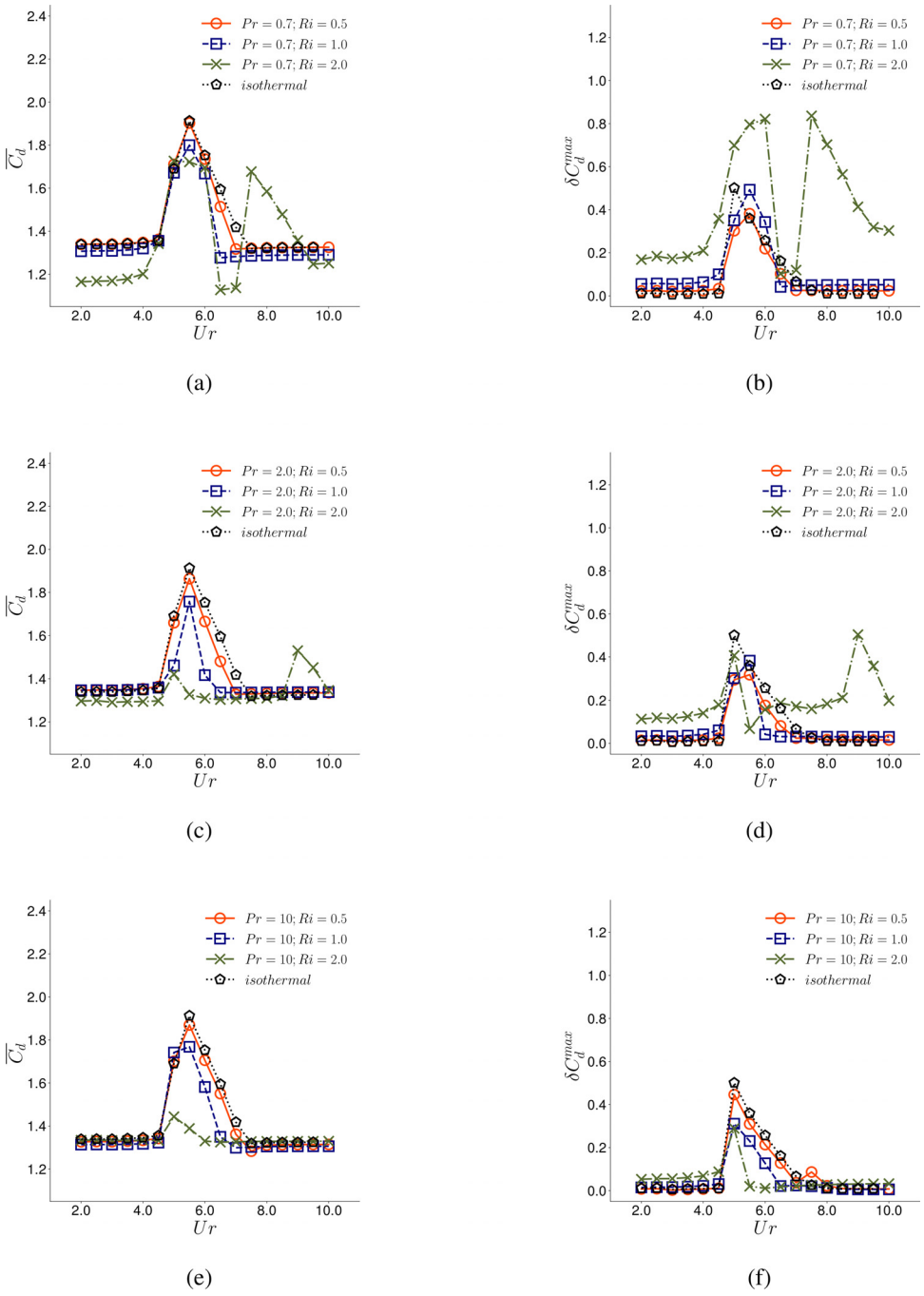

FIG. 14. Drag coefficients of a freely vibrating cylinder at $Re = 100$, $m^* = 10$, $\zeta = 0.01$, $Ur \in [2, 10]$, $Pr \in [0.7, 10]$, and $Ri \in [0.5, 2.0]$: (a), (c), and (e) the mean drag coefficient and (b), (d), and (f) the maximum fluctuation of drag coefficient.

C_e values indeed appear around the Ur values where $\phi \approx 90°$ in mixed convection. Comparing Fig. 16 with results in Fig. 17, it is further realized that either in-phase or anti-phase phase angle difference is ineffective to the kinetic transfer between fluid and structure, where very low C_e values are recorded. In addition, the responses of A_y and C_l are generally anti-phase during pre-VIV lock-in regions for different Pr and Ri values, despite that the phase angle difference is much smaller during the pre-VIV lock-in in the cases of large Pr values in Fig. 17(c). During the onset and end of kinetic energy transfer, the phase angle differences tend to switch their states, e.g., from in-phase to anti-phase

Published under an exclusive license by AIP Publishing

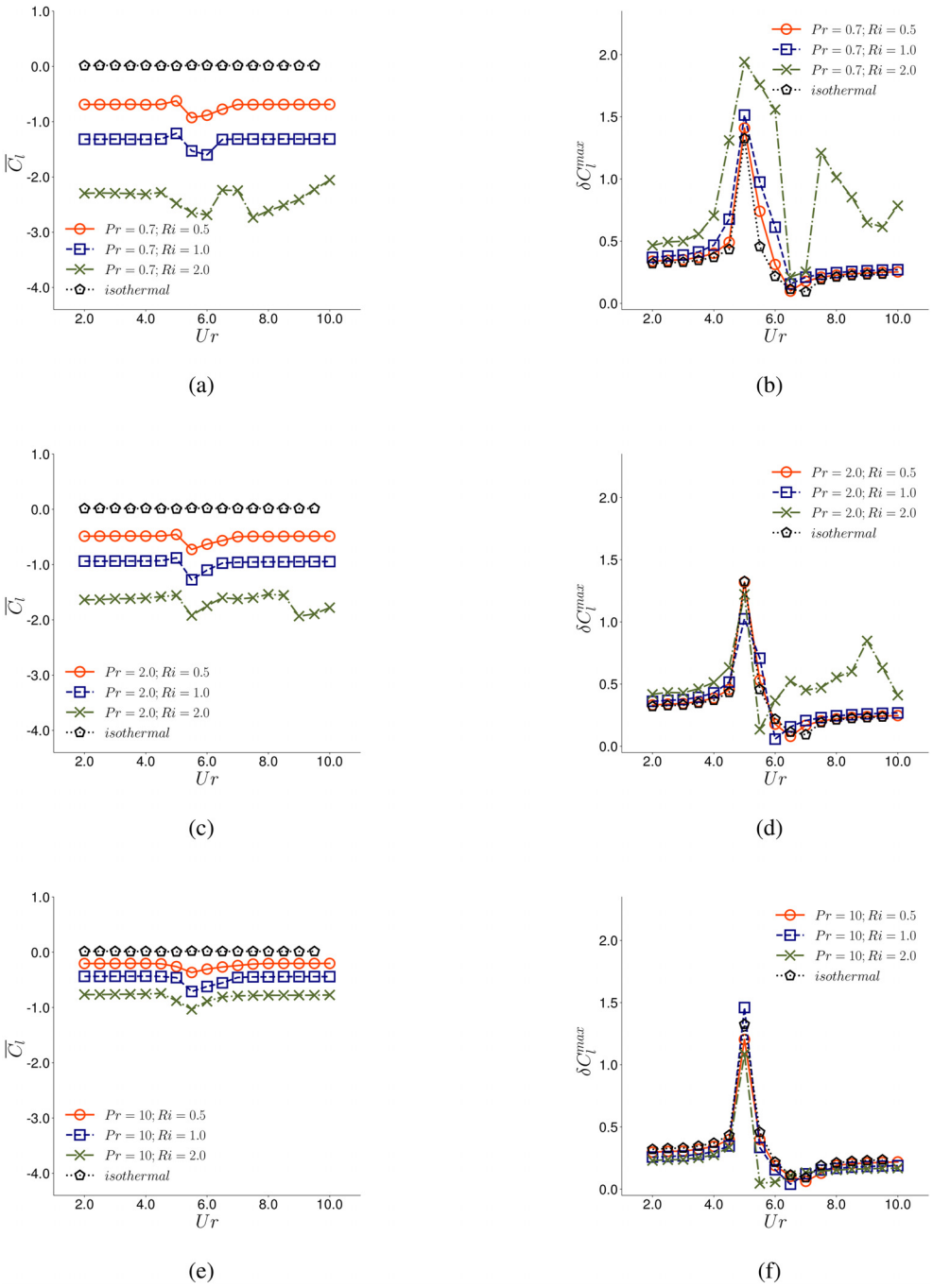

FIG. 15. Lift coefficients of a freely vibrating cylinder at $Re = 100$, $m^* = 10$, $\zeta = 0.01$, $Ur \in [2, 10]$, $Pr \in [0.7, 10]$, and $Ri \in [0.5, 2.0]$: (a), (c), and (e) the mean lift coefficient and (b), (d), and (f) the maximum fluctuation of lift coefficient.

or vice versa. The onsets of kinetic energy transfer almost occur at approximately the same reduced velocity value $Ur \approx 5.25$ for different Pr and Ri values albeit they end at very different Ur values in the cases of different Ri values. This observation agrees well with the results of C_e in Fig. 16 too. As the process of kinetic energy transfer eventually becomes suppressed further, the phase angle differences are stabilized, either in-phase or anti-phase.

Different from isothermal flow, the cross thermal buoyancy has a remarkable influence on vortex dynamics and structural dynamics in mixed convection. The perturbation of cross buoyancy to

Published under an exclusive license by AIP Publishing

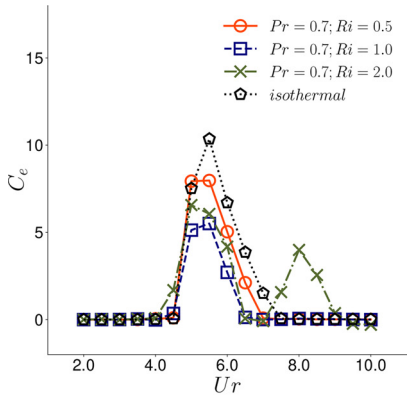

(a)

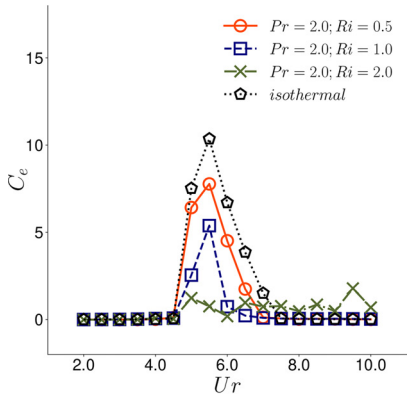

(b)

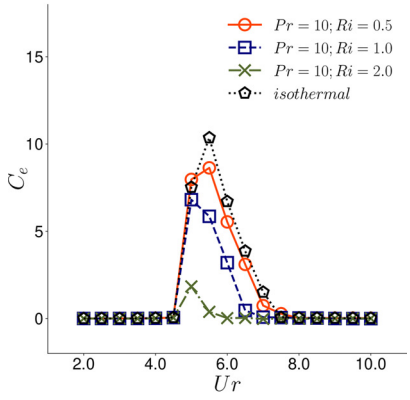

(c)

FIG. 16. Energy transfer between fluid and structure of a freely vibrating cylinder in transverse direction for $\tau \in [200, 400]$ at $Re = 100$, $m^* = 10$, $\zeta = 0.01$, and $Ur \in [2, 10]$: (a) $Pr = 0.7$ and $Ri \in [0.5, 2.0]$; (b) $Pr = 2.0$ and $Ri \in [0.5, 2.0]$ and (c) $Pr = 10$ and $Ri \in [0.5, 2.0]$.

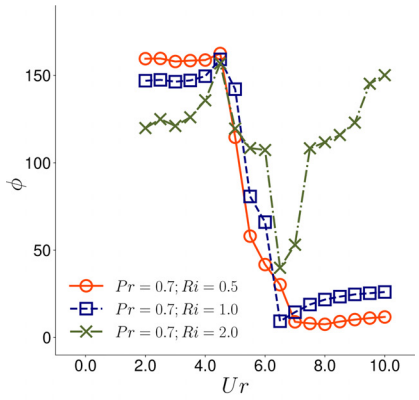

(a)

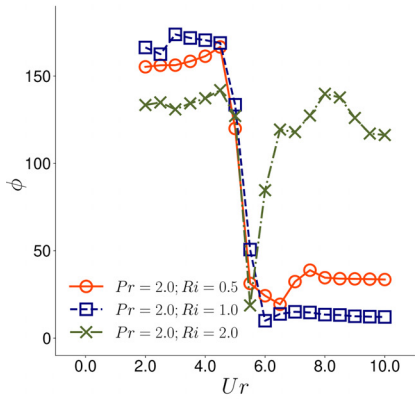

(b)

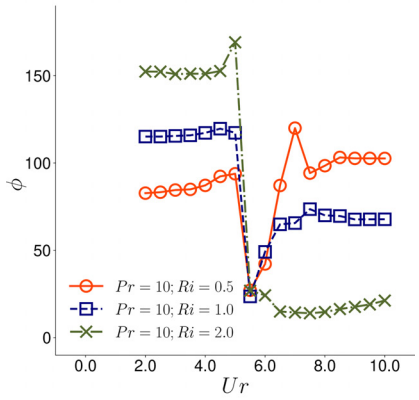

(c)

FIG. 17. Phase angle difference between transverse displacement (A_y) and lift coefficient (C_l) for a freely vibrating cylinder at $Re = 100$, $m^* = 10$, $\zeta = 0.01$, and $Ur \in [2, 10]$: (a) $Pr = 0.7$ and $Ri \in [0.5, 2.0]$; (b) $Pr = 2.0$ and $Ri \in [0.5, 2.0]$ and (c) $Pr = 10$ and $Ri \in [0.5, 2.0]$.

Published under an exclusive license by AIP Publishing

hydrodynamics and structural dynamics is subtly linked with the rate of heat convection. In this study, the heat convection rate is quantified by the value of mean Nusselt number ($\overline{Nu}$) around the cylinder's surface. Figure 18 shows that the values of $\overline{Nu}$ increase proportionally with the values of Prandtl number. This observation agrees well with the conclusion drawn in Sec. IV A, which says that the temperature contours are concentrated next to the cylinder's surface in the cases of for larger Pr values. In this study, the strongest heat convection over

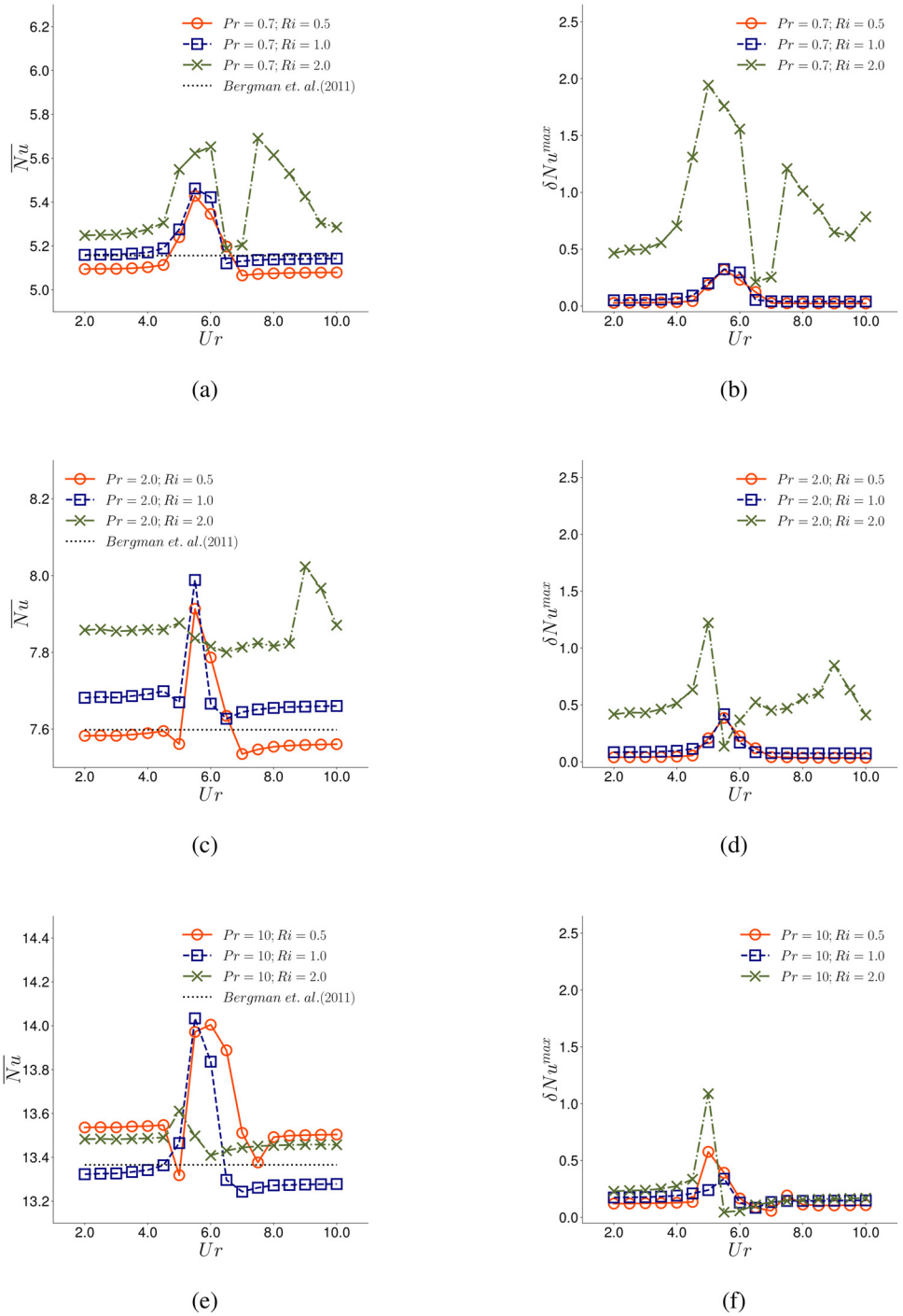

FIG. 18. Nusselt number of a freely vibrating cylinder at $Re = 100$, $m^* = 10$, $\zeta = 0.01$, $Ur \in [2, 10]$, $Pr \in [0.7, 10]$, and $Ri \in [0.5, 2.0]$: (a), (c), and (e) the mean Nusselt number and (b), (d), and (f) the maximum fluctuation of Nusselt number.

Published under an exclusive license by AIP Publishing

cylinder's surface is observed in the cases of $Pr = 10$ in Fig. 18(e). In terms of Richardson number, the value of $\overline{Nu}$ is less sensitive to the changes of buoyancy action for $Ri \in [0.5, 2.0]$, except for the cases of $Pr = 0.7$ and $Ri = 2.0$. The obtained numerical results of $\overline{Nu}$ during the off VIV lock-in states match well with the empirical formula[55,62] in Eq. (14), the dotted black horizontal line in Fig. 18. In contrast, the value of $\overline{Nu}$ becomes significantly excited by approximately 10% during VIV lock-in in the cases of different Pr and Ri values.

Unlike the values of $\overline{Nu}$, the maximum fluctuation of Nusselt number ($\delta Nu^{\max}$) is very sensitive to the changes of Richardson numbers, but insensitive to the variation of Prandtl number instead. Figures 18(b), 18(d), and 18(f) show that the responses of $\delta Nu^{\max}$ with respect to Ur values are almost identical in the cases of different Prandtl numbers and $Ri < 2.0$. The values of $\delta Nu^{\max}$ are almost zero during off VIV lock-in and merely excited by approximately 0.5 during VIV lock-in. The only exception is the cases of $Ri = 2.0$, where the

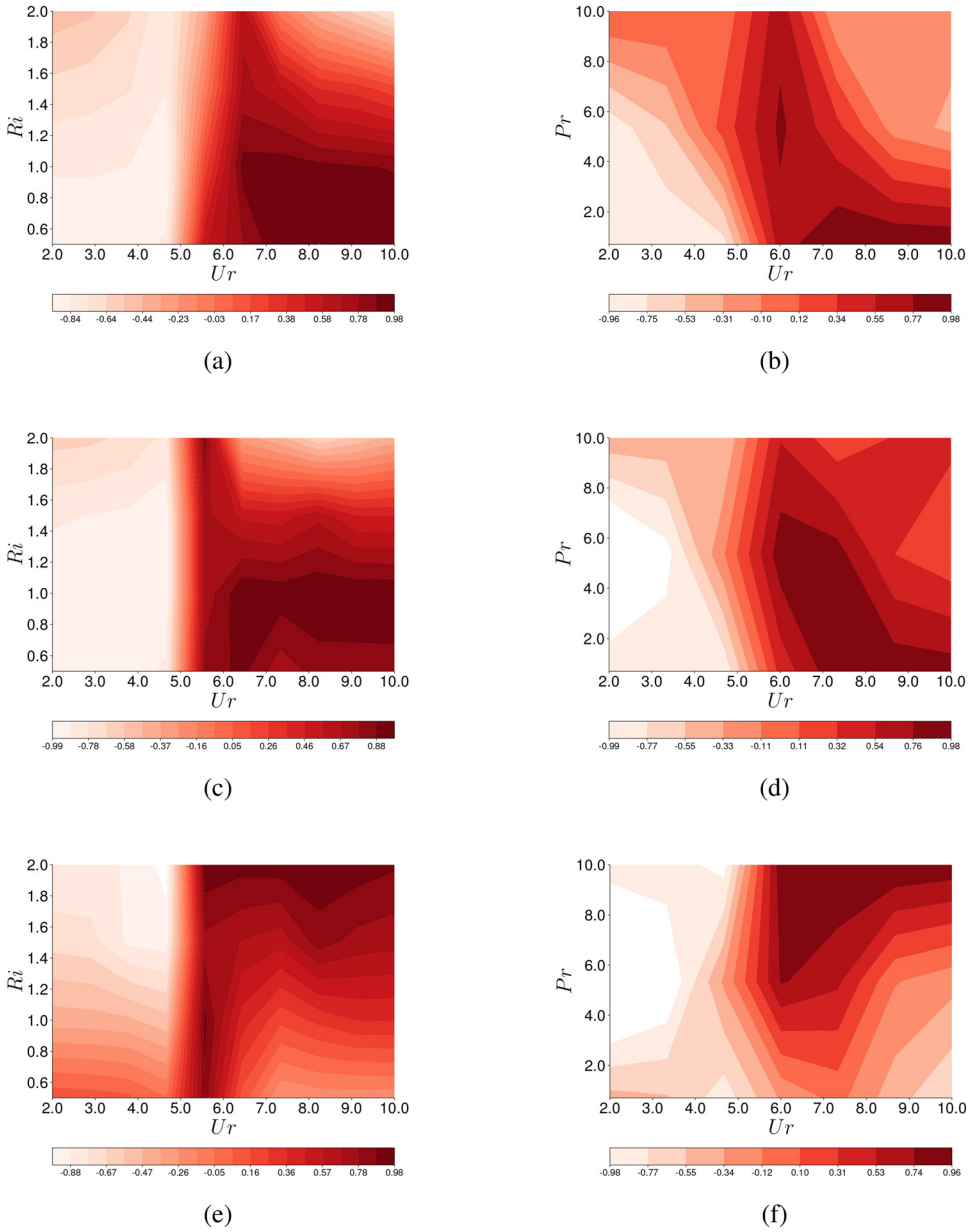

FIG. 19. Pearson's correlation between heat convection (Nu) and transverse vibration (A_y) of a freely vibrating cylinder at $Re = 100$, $m^* = 10$, $\zeta = 0.01$, and $Ur \in [2, 10]$: (a) $Pr = 0.7$ and $Ri \in [0.5, 2.0]$; (b) $Pr \in [0.7, 10]$ and $Ri = 0.5$; (c) $Pr = 2.0$ and $Ri \in [0.5, 2.0]$; (d) $Pr \in [0.7, 10]$ and $Ri = 1.0$; (e) $Pr = 10$ and $Ri \in [0.5, 2.0]$ and (f) $Pr \in [0.7, 10]$ and $Ri = 2.0$.

Published under an exclusive license by AIP Publishing

cross thermal buoyancy is strong in wake, e.g., the green dotted lines with *cross* markers in Figs. 18(b), 18(d), and 18(f). Again, the aforementioned secondary VIV lock-in for higher Ur values is affirmatively observed in the cases of $Pr = [0.7, 2.0]$ and $Ri = 2.0$. A drastic fluctuation of Nusselt number is found within the VIV lock-in states. Specifically, the maximum fluctuation of Nusselt number can achieve an amplitude as high as 2.0 in the case of $Ri = 2.0$ during VIV lock-in in Fig. 18(b). Overall, the maximum fluctuation of Nusselt number is significantly large in the cases of $Ri = 2.0$ during off VIV lock-in.

To provide an overall picture of the correlations between heat convection, structural dynamics, and hydrodynamics, we employ Pearson's correlation coefficient as an indicator to quantify their subtle relations over a range of reduced velocity ($Ur \in [2.0, 10.0]$). Figures 19(a), 19(c), and 19(e) show that heat convection and structural dynamics have strongly negative correlations during pre-lock-in ($Ur \lesssim 5.5$). As Prandtl number increases from 0.7 to 10.0, the zone of highly positive correlated heat convection and structural dynamics shifts gradually from low Richardson number to higher values.

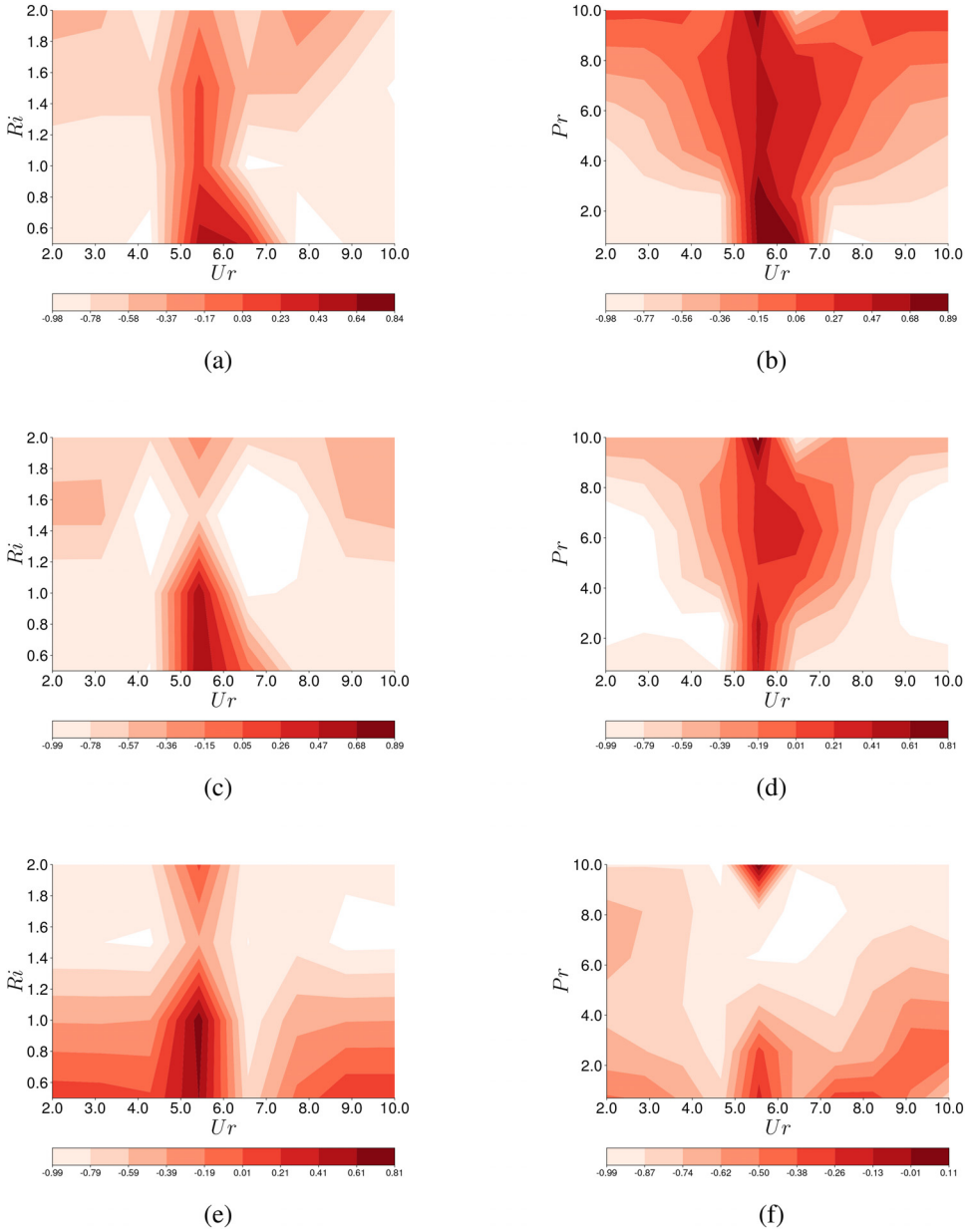

FIG. 20. Pearson's correlation between heat convection (Nu) and lift force (C_l) of a freely vibrating cylinder at $Re = 100$, $m^* = 10$, $\zeta = 0.01$, $Ur \in [2, 10]$: (a) $Pr = 0.7$ and $Ri \in [0.5, 2.0]$; (b) $Pr \in [0.7, 10]$ and $Ri = 0.5$; (c) $Pr = 2.0$ and $Ri \in [0.5, 2.0]$; (d) $Pr \in [0.7, 10]$ and $Ri = 1.0$; (e) $Pr = 10$ and $Ri \in [0.5, 2.0]$; and (f) $Pr \in [0.7, 10]$ and $Ri = 2.0$.

Published under an exclusive license by AIP Publishing

The cases of $Pr = 0.7$ and $Ur \approx 10.0$ show that their correlation is about −0.64 for $Ri = 2.0$. On the other hand, for $Pr = 10.0$ and $Ur = 10.0$, the correlation in the case of $Ri = 2.0$ becomes strongly positive (0.98) instead. Overall, highly positive correlated heat convection and structural dynamics responses can always be observed during the peak VIV lock-in stage ($Ur \approx 6.0$). On the other hand, the correlation between heat convection and transverse vibration amplitude becomes even more complex in the cases of fixed Richardson numbers in Figs. 19(b), 19(d), and 19(f). Similarly, the strong negative correlations are found during pre-VIV lock-in as well. Furthermore, the zones of highly positive correlation for $Ur \gtrsim 6.0$ shift gradually from lower Prandtl numbers to higher values, as Richardson number increases. Most of time, the heat convection and transverse vibration amplitude shows high correlation values during the peak VIV lock-in stage. Analogously, the Pearson's correlations between heat convection and lift force are plotted in Fig. 20. Unlike the correlations between Nu and A_y, the correlation between Nu and C_l merely shows apparently positive correlations during VIV lock-in in the cases of small Pr and Ri values, as plotted in Figs. 20(a), 20(c), and 20(e). Despite the overall negative correlation values manifested during the pre-VIV lock-in, the heat convection and lift force exhibit relatively high correlations for $Pr = 10.0$ and $Ri \lesssim 1.0$ over a wide range of reduced velocity values ($Ur \in [2.0, 10.0]$). It is also seen that the correlation between Nu and C_l is high during the peak VIV lock-in. However, the only exception is the case of $Ri = 2.0$, in which the values of Nu and C_l almost show negligible correlations or strongly negative correlation values in this study.

V. CONCLUSIONS

In this article, the hydrodynamic, structural, and thermal characteristics of an elastically mounted heated circular cylinder subject to cross thermal buoyancy in mixed convection were numerically investigated in the cases of $Re = 100$, $Pr \in [0.7, 10.0]$, $Ri \in [0.5, 2.0]$, and $Ur \in [0.0, 10.0]$. In those cases, both fluid inertia and cross buoyancy effect are important, but the fluid inertia is more dominant, which is of our interest. It was found that the values of mean streamwise displacement was relatively insensitive to the changes in Prandtl and Richardson numbers, but increased proportionally with the values of reduced velocity, whereas both the streamwise and transverse maximum fluctuations of cylinder were tremendously amplified during VIV lock-in. Overall, the hydrodynamics and structural dynamics in the cases of high Prandtl numbers, e.g., $Pr = 10$ in this study, were close to the values of a vibrating cylinder in isothermal flow, except for $Ri = 2.0$, where the significant perturbation by cross buoyancy effect is indispensable. Strong buoyancy action shows tremendous influence on all aspects of the results in this study, e.g., hydrodynamics, structural dynamics, and heat convection, in particular, for high reduced velocity values ($Ur \gtrsim 7.0$). The state of VIV lock-in was narrowed in the cases of larger Richardson numbers. In particular, it was noticed that VIV lock-in was almost suppressed in cases of $Pr \gtrsim 10$ and $Ri \approx 2.0$. Overall, the influence of Richardson number on structural and hydrodynamic forces was more severe than Prandtl number. This influence primarily appeared for high reduced velocity values ($Ur \gtrsim 7.0$), which was typically within the post-VIV lock-in for a freely vibrating cylinder in isothermal flow. A strong and obvious secondary VIV lock-in was reported in the cases of $Ri \approx 2.0$ and $Ur \gtrsim 7.0$. Furthermore, it also formed an extended VIV lock-in-state over a wide range of Ur values by coalescing the primary and secondary VIV lock-in states in cases of $Pr = 2.0$ and $Ri = 2.0$. The wide VIV lock-in-state was associated with a tremendous fluid kinetic energy transfer between fluid and structure, which is meaningful for the research of hydropower harvesting. Nonetheless, the fluid kinetic energy transfer could be significantly inhibited in the cases of $Pr \gtrsim 2.0$ and $Ri \approx 2.0$ instead. Similar to isothermal fluid flow, it was further confirmed that the maximum fluid kinetic energy transfer also occurred at $\phi \approx 90^\circ$ subject to cross thermal buoyancy in mixed convection and associated a phase change of the phase angle difference between lift force and transverse vibration amplitude, e.g., from in-phase to anti-phase or vice versa. In contrast, the mean Nusselt number was generally insensitive to Richardson numbers and reduced velocity albeit high values of $\overline{Nu}$ were observed during VIV lock-in and higher Prandtl numbers. Overall, it was believed that Prandtl number exhibited more influence on heat convection over the cylinder's surface. However, the maximum fluctuation of Nusselt number was apparently amplified in the cases of $Ri = 2.0$ and VIV lock-in. Finally, the Pearson's correlation was employed to obtain an overall picture of the subtle and complex relationships between heat convection, structural dynamics, and hydrodynamic forces within the parameter spaces of interest in this study.

DATA AVAILABILITY

The data that support the findings of this study are available from the corresponding author upon reasonable request.

REFERENCES

[1] S. R. De Groot, *Thermodynamics of Irreversible Processes* (North-Holland, Amsterdam, 1951), Vol. 242.
[2] J. O. Hirschfelder, C. F. Curtiss, R. B. Bird, and M. G. Mayer, *Molecular Theory of Gases and Liquids* (Wiley, NY, 1964), Vol. 165.
[3] S. Chapman and T. G. Cowling, *The Mathematical Theory of Non-Uniform Gases: An Account of the Kinetic Theory of Viscosity, Thermal Conduction and Diffusion in Gases*, 3rd ed. (Cambridge University Press, Cambridge, England, 1970).
[4] H. S. Carslaw and J. C. Jaeger, *Conduction of Heat in Solids*, 2nd ed. (Clarendon Press, Oxford, 1959).
[5] M. N. Ozisik, *Boundary Value Problems of Heat Conduction* (International Textbook Company, Scranton, 1968).
[6] M. T. Ibañez, *Advanced Boundary Elements for Heat Transfer* (Wit Pr/Computational Mechanics, 2002), Vol. 42.
[7] M. N. Özişik, H. R. Orlande, M. J. Colaco, and R. M. Cotta, *Finite Difference Methods in Heat Transfer* (CRC Press, 2017).
[8] S. Patankar, *Numerical Heat Transfer and Fluid Flow* (Taylor & Francis, 2018).
[9] R. W. Lewis, P. Nithiarasu, and K. N. Seetharamu, *Fundamentals of the Finite Element Method for Heat and Fluid Flow* (John Wiley & Sons, 2004).
[10] J. N. Reddy and D. K. Gartling, *The Finite Element Method in Heat Transfer and Fluid Dynamics* (CRC Press, 2010).
[11] G. Biswas, H. Laschefski, N. K. Mitra, and M. Fiebig, "Numerical investigation of mixed convection heat transfer in a horizontal channel with a built-in square cylinder," Numer. Heat Transfer, Part A **18**, 173–188 (1990).
[12] S. Sanitjai and R. J. Goldstein, "Heat transfer from a circular cylinder to mixtures of water and ethylene glycol," Int. J. Heat Mass Transfer **47**, 4785–4794 (2004).
[13] G. Juncu, "A numerical study of momentum and forced convection heat transfer around two tandem circular cylinders at low Reynolds numbers. Part II: Forced convection heat transfer," Int. J. Heat Mass Transfer **50**, 3799–3808 (2007).
[14] G. Biswas and S. Sarkar, "Effect of thermal buoyancy on vortex shedding past a circular cylinder in cross-flow at low Reynolds numbers," Int. J. Heat Mass Transfer **52**, 1897–1912 (2009).
[15] T. Sarpkaya, "Vortex-induced oscillations: A selective review," J. Appl. Mech. **46**, 241–258 (1979).
[16] H. M. Blackburn, R. Govardhan, and C. H. K. Williamson, "A complementary numerical and physical investigation of vortex-induced vibration," J. Fluids Struct. **15**, 481–488 (2001).

Published under an exclusive license by AIP Publishing

[17]C. H. K. Williamson and R. Govardhan, "Vortex-induced vibrations," Annu. Rev. Fluid Mech. **36**, 413–455 (2004).
[18]T. Sarpkaya, "A critical review of the intrinsic nature of vortex-induced vibrations," J. Fluids Struct. **19**, 389–447 (2004).
[19]T. Prasanth and S. Mittal, "Vortex-induced vibrations of a circular cylinder at low Reynolds numbers," J. Fluid Mech. **594**, 463–491 (2008).
[20]P. Bearman, "Circular cylinder wakes and vortex-induced vibrations," J. Fluids Struct. **27**, 648–658 (2011).
[21]H. Zhu, C. Zhang, and W. Liu, "Wake-induced vibration of a circular cylinder at a low Reynolds number of 100," Phys. Fluids **31**, 073606 (2019).
[22]H. Zhu, T. Tang, H. Zhao, and Y. Gao, "Control of vortex-induced vibration of a circular cylinder using a pair of air jets at low Reynolds number," Phys. Fluids **31**, 043603 (2019).
[23]H. Zhu, T. Tang, T. Zhou, H. Liu, and J. Zhong, "Flow structures around trapezoidal cylinders and their hydrodynamic characteristics: Effects of the base length ratio and attack angle," Phys. Fluids **32**, 103606 (2020).
[24]C. H. K. Williamson, "Evolution of a single wake behind a pair of bluff bodies," J. Fluid Mech. **159**, 1–18 (1985).
[25]M. Carini, F. Giannetti, and F. Auteri, "On the origin of the flip-flop instability of two side-by-side cylinder wakes," J. Fluid Mech. **742**, 552–576 (2014).
[26]B. Liu and R. K. Jaiman, "Interaction dynamics of gap flow with vortex-induced vibration in side-by-side cylinder arrangement," Phys. Fluids **28**, 127103 (2016).
[27]B. Liu and R. K. Jaiman, "The effect of gap flow on vortex-induced vibration of side-by-side cylinder arrangement," in *Proceedings of International Conference on Offshore Mechanics and Arctic Engineering* (American Society of Mechanical Engineers, 2016), Vol. 49934, p. V002T08A013.
[28]A. Munir, M. Zhao, H. Wu, and L. Lu, "Effects of gap ratio on flow-induced vibration of two rigidly coupled side-by-side cylinders," J. Fluids Struct. **91**, 102726 (2019).
[29]I. Borazjani and F. Sotiropoulos, "Vortex-induced vibrations of two cylinders in tandem arrangement in the proximity–wake interference region," J. Fluid Mech. **621**, 321–364 (2009).
[30]G. Assi, P. Bearman, and J. R. Meneghini, "On the wake-induced vibration of tandem circular cylinders: The vortex interaction excitation mechanism," J. Fluid Mech. **661**, 365–401 (2010).
[31]Y. Ma, W. Xu, L. Zhai, and H. Ai, "Hydrodynamic characteristics of two tandem flexible cylinders undergoing flow-induced vibration," Ocean Eng. **193**, 106587 (2019).
[32]Z. Li, W. Yao, K. Yang, R. K. Jaiman, and B. C. Khoo, "On the vortex-induced oscillations of a freely vibrating cylinder in the vicinity of a stationary plane wall," J. Fluids Struct. **65**, 495–526 (2016).
[33]B. Liu and A. R. Magee, "Numerical stability and three dimensionality of a streamline hyperbolic critical point in wake at low Reynolds number," arXiv:2006.05306 (2020).
[34]X. Ju, H. An, L. Cheng, and F. Tong, "Modes of synchronisation around a near-wall oscillating cylinder in streamwise directions," J. Fluid Mech. **893**, A8 (2020).
[35]V. Joshi, B. Liu, and R. K. Jaiman, "Flow-induced vibrations of riser array system," in *Proceedings of International Conference on Offshore Mechanics and Arctic Engineering* (American Society of Mechanical Engineers, 2016), Vol. 49934, p. V002T08A012.
[36]T. Tang, P. Yu, X. Shan, J. Li, and S. Yu, "On the transition behavior of laminar flow through and around a multi-cylinder array," Phys. Fluids **32**, 013601 (2020).
[37]K. Venkatasubbaiah and T. K. Sengupta, "Mixed convection flow past a vertical plate: Stability analysis and its direct simulation," Int. J. Therm. Sci. **48**, 461–474 (2009).
[38]T. K. Sengupta and T. Poinsot, *Instabilities of Flows: With and Without Heat Transfer and Chemical Reaction* (Springer Science & Business Media, 2010), Vol. 517.
[39]T. K. Sengupta, S. Unnikrishnan, S. Bhaumik, P. Singh, and S. Usman, "Linear spatial stability analysis of mixed convection boundary layer over a heated plate," Prog. Appl. Math. **1**, 71–89 (2011).
[40]T. K. Sengupta, *Instabilities of Flows and Transition to Turbulence* (CRC Press, 2012).
[41]E. Izadpanah, Y. Amini, and A. Ashouri, "A comprehensive investigation of vortex induced vibration effects on the heat transfer from a circular cylinder," Int. J. Therm. Sci. **125**, 405–418 (2018).
[42]H. Garg, A. K. Soti, and R. Bhardwaj, "Vortex-induced vibration of a cooled circular cylinder," Phys. Fluids **31**, 083608 (2019).
[43]H. Garg, A. K. Soti, and R. Bhardwaj, "Vortex-induced vibration and galloping of a circular cylinder in presence of cross-flow thermal buoyancy," Phys. Fluids **31**, 113603 (2019).
[44]M. A. Khan, S. F. Anwer, S. A. Khan, and N. Hasan, "Hydrodynamic and heat transfer characteristics of vortex-induced vibration of square cylinder with various flow approach angle," Int. J. Therm. Sci. **156**, 106454 (2020).
[45]Z. Yang, L. Ding, L. Zhang, L. Yang, and H. He, "Two degrees of freedom flow-induced vibration and heat transfer of an isothermal cylinder," Int. J. Heat Mass Transfer **154**, 119766 (2020).
[46]B. Liu and R. K. Jaiman, "Dynamics and stability of gap-flow interference in a vibrating side-by-side arrangement of two circular cylinders," J. Fluid Mech. **855**, 804–838 (2018).
[47]W. G. Dettmer and D. Perić, "A new staggered scheme for fluid–structure interaction," Int. J. Numer. Methods Eng. **93**, 1–22 (2013).
[48]A. N. Brooks and T. J. R. Hughes, "Streamline upwind/Petrov–Galerkin formulations for convection dominated flows with particular emphasis on the incompressible Navier–Stokes equations," Comput. Methods Appl. Mech. Eng. **32**, 199–259 (1982).
[49]T. J. Hughes, L. P. Franca, and M. Balestra, "A new finite element formulation for computational fluid dynamics: V. Circumventing the Babuška–Brezzi condition: A stable Petrov–Galerkin formulation of the Stokes problem accommodating equal-order interpolations," Comput. Methods Appl. Mech. Eng. **59**, 85–99 (1986).
[50]J. G. Heywood, R. Rannacher, and S. Turek, "Artificial boundaries and flux and pressure conditions for the incompressible Navier–Stokes equations," Int. J. Numer. Methods Fluids **22**, 325–352 (1996).
[51]K. Stein, T. Tezduyar, and R. Benney, "Mesh moving techniques for fluid-structure interactions with large displacements," J. Appl. Mech. **70**, 58–63 (2003).
[52]J. Chung and G. M. Hulbert, "A time integration algorithm for structural dynamics with improved numerical dissipation: The generalized-α method," J. Appl. Mech. **60**, 371–375 (1993).
[53]K. E. Jansen, C. H. Whiting, and G. M. Hulbert, "A generalized-α method for integrating the filtered Navier–Stokes equations with a stabilized finite element method," Comput. Methods Appl. Mech. Eng. **190**, 305–319 (2000).
[54]S. Sarkar, A. Dalal, and G. Biswas, "Unsteady wake dynamics and heat transfer in forced and mixed convection past a circular cylinder in cross flow for high Prandtl numbers," Int. J. Heat Mass Transfer **54**, 3536–3551 (2011).
[55]S. W. Churchill and M. Bernstein, "A correlating equation for forced convection from gases and liquids to a circular cylinder in crossflow," J. Heat Transfer **99**, 300–306 (1977).
[56]L. Lu, J.-M. Qin, B. Teng, and Y.-C. Li, "Numerical investigations of lift suppression by feedback rotary oscillation of circular cylinder at low Reynolds number," Phys. Fluids **23**, 033601 (2011).
[57]B. Liu and D. Tan, "A Nitsche stabilized finite element method for embedded interfaces: Application to fluid-structure interaction and rigid-body contact," J. Comput. Phys. **413**, 109461 (2020).
[58]S. Mittal and S. Singh, "Vortex-induced vibrations at subcritical Re," J. Fluid Mech. **534**, 185 (2005).
[59]D. I. Dolci and B. S. Carmo, "Bifurcation analysis of the primary instability in the flow around a flexibly mounted circular cylinder," J. Fluid Mech. **880**, R5 (2019).
[60]Y. Bao, C. Huang, D. Zhou, J. Tu, and Z. Han, "Two-degree-of-freedom flow-induced vibrations on isolated and tandem cylinders with varying natural frequency ratios," J. Fluids Struct. **35**, 50–75 (2012).
[61]N. E. Huang, *Hilbert-Huang Transform and Its Applications* (World Scientific, 2014), Vol. 16.
[62]H. Zhu, J. Zhong, and T. Zhou, "Wake structure characteristics of three tandem circular cylinders at a low Reynolds number of 160," Phys. Fluids **33**, 044113 (2021).

Published under an exclusive license by AIP Publishing